arXiv:2009.01194v2 [cs.CE] 29 Oct 2020

Accelerated reactive transport simulations in heterogeneous porous medium using Reaktoro and Firedrake

Svetlana Kyas[a*] matcules@ethz.ch
Diego Volpatto[b] volpatto@lncc.br
Martin O. Saar[a] saarm@ethz.ch
Allan M. M. Leal[a] allan.leal@erdw.ethz.ch

[a] *Institute of Geophysics, Department of Earth Sciences, ETH Zürich, Switzerland*
[b] *National Laboratory for Scientific Computing, Brazil*

Abstract

Geochemical reaction calculations in reactive transport modeling are costly in general. They become more expensive the more complex is the chemical system and the activity models used to describe the non-ideal thermodynamic behavior of its phases. Accounting for many aqueous species, gases, and minerals also contributes to more expensive computations. This work investigates the performance of the *on-demand machine learning (ODML) algorithm* presented in Leal et al. (2020) when applied to different reactive transport problems in heterogeneous porous media. We demonstrate that the ODML algorithm enables faster chemical equilibrium calculations by one to three orders of magnitude. This, in turn, significantly accelerates the entire reactive transport simulations. The numerical experiments are carried out using the coupling of two open-source software packages: Firedrake (Rathgeber et al., 2016) and Reaktoro (Leal, 2015).

1 Introduction

Modeling coupled physical and chemical processes is not only scientifically challenging but also computationally demanding due to the high computing costs of chemical reaction calculations. The importance of reactive transport modeling has significantly increased over the past years due to becoming essential for understanding the processes occurring in surface or subsurface systems as well as engineering and environmental problems. Applications include a wide variety of geochemical processes. Among many are rock/mineral alteration in natural diagenetic systems as a response to carbon capture and geological sequestration and chemical stimulation of an enhanced geothermal reservoir, injection of acid gases resulting in groundwater contamination, enhanced

*Corresponding author

oil and gas recovery, transport, and storage of radiogenic and toxic waste products in geological formations, and the study of deep Earth processes such as metamorphism and magma transport (see Steefel et al. 2005; Xiao et al. 2018; Steefel 2019 and references therein). Both chemical and physical processes are strongly coupled, meaning that chemical reactions alter fluid and rock composition. Such coupling changes the physical and chemical properties of the modeled fluids and the porous medium (e.g., rock porosity and permeability, fluid density, and viscosity), ultimately affecting how fluids, heat, and chemical species are transported.

Depending on the particular reactive transport system in question, chemical reactions in fluid flow simulations can account for the majority of computational costs. Achieving a more balanced cost distribution is usually a challenging task, given the nature of the computations for the complex chemical system. Simulation of the physical processes usually leads to solving sparse systems of linear algebraic equations that result from the discretization of partial differential equations (PDEs) governing conservation laws. The computing cost for modeling chemical processes, in turn, is comprised of several steps, i.e., (i) computation of thermodynamic properties of tens to hundreds of species using complex equations of state that model the non-ideal behavior of fluid and solid phases; (ii) solution of a system of non-linear differential-algebraic equations to calculate chemical equilibrium or kinetic states. These operations must be repeated in all discretization cells of the computational domain, at each time step of the reactive transport simulation.

The classical/conventional algorithms for chemical equilibrium calculations include those based on the *Gibbs energy minimization* (GEM) approach and the *law of mass action* (LMA) equations, also known in the literature as *non-stoichiometric* and *stoichiometric methods,* respectively (Smith and Missen, 1982). They are fundamentally equivalent (Smith and Missen, 1982; Zeleznik and Gordon, 1960), except that the standard chemical potentials of species are used in the GEM method. In turn, in the LMA methods, equilibrium constants of reactions are expected. A practical conversion technique between these two data types is shown in Leal et al. (2016) to enable GEM algorithms to take advantage of many existing LMA databases.

The most commonly-used simulators for reactive transport simulations include the packages presented in the following list: PHREEQC (Parkhurst and Appelo, 1999), CORE2D (Samper et al., 2000), OpenGeoSys (OGS) (Jang et al., 2018; Lichtner et al., 2019), HYTEC (Simunek and van Genuchten, 2014), ORCHESTRA (Meeussen, 2003), Frachem (Bächler and Kohl, 2005), TOUGHREACT (Xu et al., 2006), eSTOMP (White and Oostrom, 2006), The Geochemist's Workbench (Bethke, 2007), GEM-Selektor and GEMS3K (Kulik et al., 2004, 2013), HYDROGEOCHEM (Yeh et al., 2013), PROOST (Gamazo et al., 2016), CrunchFlow (Steefel, 2009) , MIN3P (Mayer, 2020), PFLOTRAN (Lichtner et al., 2019), and MODFLOW (Langevin et al., 2019) among many others. A more exhaustive overview of these packages capabilities, along with a list of applications, has been provided in Steefel et al. (2015). For more details, the interested reader is referred to the web-pages, user manuals, or publications cited for the specific codes.

Given the inherent complexity of modeling physical and chemical processes individually, reactive transport codes are often a combination of specialized packages (i.e., one for the physics and another for the chemistry). Several examples of such coupling are given next: HP1/HPx (Jacques and Simunek, 2005) (as the coupling of HYDRUS, Simunek and van Genuchten 2008, and PHREEQC, Parkhurst and Appelo 2013); PHT3D (as the coupling of MT3DMS, Zheng and Wang 1999, and PHREEQC); COMSOL-PHREEQC iCP; (Nardi et al., 2014), COMSOL-PHREEQC (Guo et al., 2018); COMSOL-GEMS (Azad et al., 2016); CSMP++GEM (Yapparova et al., 2017); DuCOM-Phreeqc (Elakneswaran and Ishida, 2014); GeoSysBRNS (Centler et al., 2010); Matlab-IPhreeqc

(Muniruzzaman and Rolle, 2016); OGS-Chemapp (Li et al., 2014); OGS-GEM (Kosakowski and Watanabe, 2014); OGS-IPhreeqc (He et al., 2015); ReactMiCP (Georget et al., 2017); ReacTran (Guo et al., 2018); TReacLab (Jara et al., 2017). A detailed overview of the advantages and limitations of these packages is presented in Gamazo et al. (2016) and Damiani et al. (2020).

In this work, we present a novel coupling of the packages Reaktoro (Leal, 2015) and Firedrake (Rathgeber et al., 2016) for modeling reactive transport processes with *the on-demand machine learning (ODML) acceleration strategy* (Leal et al., 2020). This strategy can substantially speed up the geochemical reaction calculations in reactive transport simulations by orders of magnitude. The main idea is to *learn essential chemical equilibrium calculations during the simulation so that we can perform fast and accurate predictions of the subsequent ones.* Comprehensive evaluations made during the learning stage will also be referred to as *conventional or full evaluations* of chemical equilibrium states throughout the paper, whereas the predictions will alternatively be called *smart estimations* or *smart predictions*. The on-demand learning is *triggered* only when the previously learned calculations are insufficient to produce accurate approximation for the new equilibrium states. This way, instead of performing millions to billions of full and expensive chemical equilibrium calculations, we typically require only a few hundreds to thousands of them. The *on-demand learning operation* can be performed by either a Gibbs energy minimization (GEM) or by a law of mass action (LMA) algorithm. This paper provides further demonstration, in addition to those presented in Leal et al. (2020), of the potential of the ODML algorithm to substantially accelerate reactive transport simulations. We now consider more complex chemical systems and/or geologic features in the simulations, i.e., two-dimensional (2D) porous media with heterogeneity compared to those shown in Leal et al. (2020).

Reaktoro is a computational framework developed in C++ and Python for modeling chemically reactive processes governed by either chemical equilibrium, chemical kinetics, or a combination of both. For chemical equilibrium calculations, Reaktoro implements numerical methods based on *Gibbs energy minimization* (GEM) (Leal et al., 2014, 2016, 2017) or based on an *extended law of mass action* (xLMA) formulation (Leal et al., 2016) that combines the advantages of both GEM and LMA methods. For chemical kinetics calculations, with partial chemical equilibrium considerations, the algorithm presented in Leal et al. (2015) is used, which adopts an implicit time integration scheme for enhanced stability in combination with adaptive time stepping strategy for efficient simulation of chemical kinetics. The on-demand machine learning (ODML) algorithm for faster chemical equilibrium calculations was introduced recently in Reaktoro (Leal et al., 2020).

Firedrake is an open-source library for solving PDEs with finite element methods (FEM). It is used here to solve the equations that govern (solute/heat) transport processes (advection/diffusion equations) and fluid flow (i.e., the Darcy equation). The package utilizes a high-level expressive domain-specific language (DSL) embedded in Python called Unified Form Language (UFL) (Alnæ s et al., 2014), which provides symbolic representations of variational problems corresponding to the PDEs that govern physical laws. Besides, it presents a simple public API to avoid the UFL abstraction. This configuration allows users to implement mathematical operations that fall outside common variational formulations.

Note: It is worth remarking that a similar software coupling is rather straightforward with another open-source computing platform for solving PDEs, the FEniCS Project (Logg and Wells, 2010, 2012). Examples using such coupling can be found in Damiani et al. (2020). Besides Firedrake and the FEniCS Project, Reaktoro has also been coupled with OpenFOAM (Jasakh, 2012) to produce the pore-scale reactive transport simulator poroReact (Oliveira et al., 2019).

This communication is organized as follows. **Section 2** presents the governing equations for the physical and chemical processes considered in the following reactive transport simulations. **Section 3** provides an overview of the numerical methods used in Reaktoro and Firedrake. **Section 4** describes two reactive transport simulations conducted with Reaktoro and Firedrake and discusses the numerical performance of the ODML approach when applying it to 2D heterogeneous problems. In **Section 5,** we summarize the obtained results, draw conclusions, and discuss the future work planned.

2 Governing equations

This section presents the governing equations for the physical and chemical processes considered in the reactive transport simulations of Section 4. Due to the complexity of each process, our presentation is organized into three parts:

1. *single-phase fluid flow in porous medium* (Subsection **2.1***);*
2. *reactive transport of the fluid species* (Subsection **2.2***);*
3. *chemical reactions among the fluid and solid species* (Subsection **2.3***).*

2.1 Single-phase fluid flow in porous medium

For the sake of investigating the performance of the ODML algorithm to speed up chemical equilibrium calculations in reactive transport simulations, it suffices to have a relatively simpler model for fluid flow. Such a choice can be justified by our primary concern on how the ODML behaves with slightly more complex chemical systems and heterogeneous porous media. Thus, we assume that the fluid is incompressible, gravity effects are negligible, and the porous medium is isotropic and nondeformable. Given these assumptions, we solve the coupled **continuity equation** and the **Darcy equation** below to compute the fluid pressure P and fluid Darcy velocity $\boldsymbol{u}$ throughout the medium:

$$\nabla \cdot (\rho \boldsymbol{u}) = f \qquad \text{in } \Omega \times (0, t_{\text{final}}), \tag{1}$$

$$\boldsymbol{u} = -\frac{\kappa}{\mu} \nabla P \qquad \text{in } \Omega \times (0, t_{\text{final}}). \tag{2}$$

Here, ρ and μ are the density and the dynamic viscosity of the fluid, f is the rate of fluid injection/production, $\kappa = \kappa(\boldsymbol{x})$, $\boldsymbol{x} \in \Omega$, is the (isotropic) permeability field of the porous rock, Ω is the physical domain, and t_{final} is the final time of the simulation.

2.2 Reactive transport of the fluid species

The fluid species in the chemical system are subject to the mass conservation law as they advect, diffuse, and disperse through the porous media, while simultaneously reacting with the rock minerals. We use the mathematical formulation presented in Appendix 4 of Leal et al. (2020) for the reactive transport of fluid species in terms of chemical element amounts. This approach is a standard procedure in the literature that substantially reduces the total number of PDEs to be solved

for transport phenomena (Lichtner, 1985). The formulation also accounts for the dissolution and precipitation of the solid species and read as

$$\frac{\partial(b_j^{\mathrm{f}} + b_j^{\mathrm{s}})}{\partial t} + \nabla \cdot (\boldsymbol{v} b_j^{\mathrm{f}} - D \nabla b_j^{\mathrm{f}}) = 0 \qquad (j = 1, \ldots, \mathrm{E}), \tag{3}$$

where b_j^{f} and b_j^{s} are the amounts of the elements in the fluid and the solid, respectively. Here, D is the dispersion-diffusion tensor (Peaceman, 1977), i.e.,

$$D = (\alpha_{\mathrm{mol}} + \alpha_{\mathrm{t}} |\boldsymbol{u}|) I + \frac{\alpha_{\mathrm{l}} - \alpha_{\mathrm{t}}}{|\boldsymbol{u}|} \boldsymbol{u} \otimes \boldsymbol{u} \tag{4}$$

where α_{mol} is the molecular diffusion coefficient and α_{l} and α_{t} are the longitudinal and the transversal dispersion coefficients, respectively.

Note: We assume that α_l and α_t are both zero so that $D \equiv \alpha_{\mathrm{mol}}$, which suffices for the numerical investigations of the on-demand machine learning (ODML) algorithm performance in Section 4. Finally, r_i^{f} and r_i^{s} are respectively the rates of production/consumption of the ith fluid and solid species (in mol/s) due to chemical reactions among themselves.

Equation (3) has two advantages when compared to the transport equation for chemical species:

- Absence of the reaction term in the convection-diffusion equation, leaving such concerns to a separate chemical kinetic/equilibrium solver and easing the coupling procedure.
- A considerable decrease in the number of unknowns, since the number of chemical elements is usually much less than the number of chemical species.

Note: For more than one fluid phase (each with its velocity field) and different diffusion coefficients for the fluid species, this simplified transport formulation becomes less straightforward.

2.3 Chemical reactions among the fluid and solid species

In our simulations, homogeneous and heterogeneous chemical reactions among the species are considered (i.e. reactions among fluid species and between fluid and solid species). We adopt a *local chemical equilibrium model* so that both fluid and solid species are in chemical equilibrium at any point in space and time. Because of transport processes and variations in temperature/ pressure (when applicable), the chemical equilibrium states are continually altered at each point of the domain. For example, a rock mineral may gradually dissolve as the more acidic fluid passes through that point in space.

Thus, at every discretized point in space, we solve the Gibbs energy minimization problem:

$$\min_n G(T, P, n) \quad \text{subject to} \quad \begin{cases} An = b \\ n \geq 0 \end{cases}, \tag{5}$$

to compute the *chemical equilibrium amounts* $n = (n_1, \ldots, n_{\mathrm{N}})$ of the species distributed among all fluid and solid phases in the chemical system. This includes the amounts of the aqueous species (solute and solvent water) and the amounts of all considered minerals that compose the porous rock. **Note:** This chemical equilibrium problem requires the temperature T, pressure P and

the amounts of chemical elements and electric charge $b = (b_1, \ldots, b_{\mathrm{E}})$ in each discretized point in space, with T assuming a uniform value throughout the medium, P computed via the solution of the continuity and Darcy equations, and b updated over time via the reactive transport equations shown in the previous section. For more information about the procedure for minimization of Gibbs energy, including information about the mass balance constraints $An = b$ and non-negative constraints $n \geq 0$, we refer to Leal et al. (2020, 2017).

3 Numerical methods

In this section, we consider the numerical methods required to solve the governing equations presented in the previous section. To solve the fluid flow through a heterogeneous porous medium, we use a highly conservative and consistent finite element method (FEM) to capture the velocity field accurately. The transport equations are solved with a suitable FEM that handles advection-dominated flow. For the multiphase chemical equilibrium calculations, involving the fluid and solid species, a Gibbs energy minimization algorithm is employed (Leal et al., 2016, 2017). In addition to these numerical methods, we also provide a brief review of the on-demand machine learning algorithm (ODML) presented in Leal et al. (2020). It is applied to accelerate several millions of expensive equilibrium calculations in the course of the reactive transport simulation. This sheer number of calculations is a result of the need to compute equilibrium states at each mesh point (*or degree of freedom* (DOF) in the finite element naming convention) during each time step.

3.1 Staggered operator splitting steps

To solve the time-dependent reactive transport equations in (3), we apply the fully-discrete formulation resulting from a combination of the finite difference approximation in time with the finite element approach in space. Let k denote the current *time-step* and $\Delta t = t^{k+1} - t^k$ the *time-step length* used in the uniform discretization $I_{\Delta t} := \{0 = t_0 < t_1 < \ldots < t_K = t_{\mathrm{final}}\}$ of the time interval $[0, t_{\mathrm{final}}]$, where $t_{\mathrm{final}} > 0$ is the total time. We perform the following *operator splitting* procedure at the kth time-step:

I. Consider (3) using the *backward Euler scheme in time* and compute an intermediate approximation of the element concentrations in the fluid partition $\tilde{b}_j^{\mathrm{f,\,k+1}} = \tilde{b}_j^{\mathrm{f}}(t_{k+1})$, $j = 1, \ldots, \mathrm{E}$:

$$\frac{\tilde{b}_j^{\mathrm{f},k+1} - \tilde{b}_j^{\mathrm{f},k}}{\Delta t} + \nabla \cdot (\boldsymbol{u}\tilde{b}_j^{\mathrm{f},k+1} - D\nabla\tilde{b}_j^{\mathrm{f},k+1}) = 0 \qquad \text{in} \quad \Omega. \tag{6}$$

We assume the flux boundary condition on the *inlet face of boundary* $\Gamma_{\mathrm{inlet}} \subset \partial\Omega$, where we inject the brine,

$$-(\boldsymbol{u}\tilde{b}_j^{\mathrm{f},k+1} - D\nabla\tilde{b}_j^{\mathrm{f},k+1}) \cdot \boldsymbol{n}_{\mathrm{inlet}} = u\hat{b}_{j,\mathrm{inlet}} \quad \text{on} \quad \Gamma_{\mathrm{inlet}}$$

and zero flux on the top and bottom of the boundary, $\Gamma_{\mathrm{top}}, \Gamma_{\mathrm{bottom}} \subset \Gamma \equiv \partial\Omega$,

$$-(\boldsymbol{u}\tilde{b}_j^{\mathrm{f},k+1} - D\nabla\tilde{b}_j^{\mathrm{f},k+1}) \cdot \boldsymbol{n} = 0 \quad \text{on} \quad \Gamma_{\mathrm{top}} \cup \Gamma_{\mathrm{bottom}}.$$

The right boundary is considered a free (open) outflow boundary. Here, $\boldsymbol{n}$ is the outward-pointing normal vector on the boundary face Γ ($\boldsymbol{n}_{\mathrm{inlet}}$ is $\boldsymbol{n}$ on Γ_{inlet}), and $\hat{b}_{j,\mathrm{inlet}}$ (in $\mathrm{mol/m^3_{fluid}}$)

is the imposed concentration of the jth element in the injected fluid. As a space discretization solver for (6), we use the Streamline-Upwind Petrov-Galerkin (SUPG) scheme introduced in Brooks and Hughes (1982) (see details in Section 3.3) to handle advection-dominated transport (of chemical species) in a particularly accurate and stable way.

Generally, the velocity in (6) is generated from the coupling to the Darcy problem, i.e., $\boldsymbol{u} = \boldsymbol{u}^k$, where $\boldsymbol{u}^k$ satisfies the system

$$\begin{aligned} \nabla \cdot (\varrho \boldsymbol{u}^k) &= f^k && \text{in} \quad \Omega \times (0, \mathrm{t}_{\text{final}}), \\ \boldsymbol{u}^k &= -\tfrac{\kappa}{\mu} \nabla P^k && \text{in} \quad \Omega \times (0, \mathrm{t}_{\text{final}}). \end{aligned} \tag{7}$$

A complete numerical analysis, demonstrating the existence and uniqueness of the solution for the above semi-discrete system, can be found in Malta and Loula (1998); Malta et al. (2000).

II. Update the total concentrations of each element b_j, using previously computed intermediate concentrations of each element $\tilde{b}_j^{\mathrm{f},k+1}$ and assuming that the element concentration in the solid partition b_j^{s} remains constant during the transport step:

$$b_j^{k+1} = \tilde{b}_j^{\mathrm{f},k+1} + b_j^{\mathrm{s},k}. \tag{8}$$

III. Calculate concentrations of the species n_i^{k+1} in each mesh cell for given *T, P,* and *updated local concentrations of elements* b_j^{k+1} using the smart chemical equilibrium algorithm accelerated with the ODML strategy (see Section 3.4).

To make sure that the Courant–Friedrichs–Lewy (CFL) condition is satisfied, we assume CFL = 0.3 and the time step is defined by

$$\Delta t = \frac{\mathrm{CFL}}{\max\left\{\max|v_x|/\Delta x, \max|v_y|/\Delta y\right\}}, \tag{9}$$

where $v = [v_x; v_y]^{\mathrm{T}}$, and Δx and Δy are the lengths of the cells along the x and y coordinates, respectively.

3.2 SDMH method for fluid flow in porous

In the following, we briefly describe the relevant part of the finite element method (FEM) applied in the present work. We use a conservative FEM to obtain accurate velocity fields that satisfy mass conservation, an important numerical feature for transport problems in heterogeneous media. The formulation is based on stabilized mixed finite element methods (Brezzi and Fortin, 2001; Masud and Hughes, 2002; Correa and Loula, 2008) combined with hybridization techniques (Cockburn and Gopalakrishnan, 2004; Cockburn et al., 2009). The resulting *Stabilized Dual Hybrid Mixed (SDHM)* method (Núñez et al., 2012) has all Discontinuous Galerkin (DG) desirable features while requiring fewer degrees of freedom (DOF) due to the static condensation procedure. The discretized global system is solved for Lagrange multipliers only (defined on the mesh skeleton), and the solution for pressure and velocity fields is recovered by the element-wise post-processing of these multipliers' solution. For the derivation of the scheme, we refer the reader to Appendix A.

3.3 SUPG method for semi-discrete element-based transport problem

To find the approximation of the semi-discrete transport problem, we choose the Streamline Upwind Petrov-Galerkin (SUPG) method. Usually, it is applied to advection-dominated partial differential equations to suppress numerical oscillations present in the classical Petrov-Galerkin method for this class of a problem (Brooks and Hughes, 1982). The weak formulation of (3) with the chosen stabilization term and all the parameters needed for its definition are discussed in detail in Appendix B**.**

3.4 Smart chemical equilibrium calculation method

Finally, we briefly describe the *smart chemical equilibrium calculations method* presented in Leal et al. (2020), which combines a classical/conventional algorithm for chemical equilibrium with an *on-demand machine learning* (ODML) strategy that speeds up the calculations by one to three orders of magnitude (dependending on the characteristics of the considered problem). Let the process of solving the mathematical problem in (5) (i.e., the problem of computing a chemical equilibrium state) be represented in the following functional notation:

$$y = f(x), \tag{10}$$

where $\boldsymbol{f}$ is the function that performs the necessary steps towards a solution, and x and y are the *input and output vectors* (not related to spatial variables) defined as

$$x = \begin{bmatrix} T \\ P \\ b \end{bmatrix} \qquad \text{and} \qquad y = \begin{bmatrix} n \\ \mu \end{bmatrix}. \tag{11}$$

Here, x is comprised of temperature (T), pressure (P), and the amount of each element in the chemical system (vector b). Vector y contains the final amount of each species in the chemical system (vector n) after they were allowed to react for the given time interval. In addition to this, it includes the vector of the chemical potentials of the species μ. In other words, y contains the information on the final speciation of the chemical system and thermochemical properties at that final state. Assume that f has been evaluated previously with input conditions $\mathring{x}$, such that $\mathring{y} = f(\mathring{x})$, and a new evaluation needs to be performed with x instead. Rather than computing y, which requires an expensive evaluation of function f, we first try estimating it using *the first-order Taylor extrapolation*

$$\tilde{y} = y + \mathring{y}_x(x - \mathring{x}), \tag{12}$$

where $\mathring{y}$ is an estimate of the exact $y = f(x)$, and $\mathring{y}_x := \partial f/\partial \mathring{x}$ is the Jacobian matrix of f evaluated at the reference input point $\mathring{x}$. We also refer to $\partial f/\partial \mathring{x}$ as the *chemical state's sensitivity matrix* at a value $\mathring{x}$ because it characterizes how sensitive the final computed chemical state is with respect to the change in temperature, pressure, and the amounts of elements. Thus, we can use $\mathring{y}_x$ to estimate how the species amounts in the final state would change when small perturbations are applied to T,P, and b. Such sensitivities can be used to predict new chemical equilibrium states quickly and accurately in the vicinity of some previously and thoroughly calculated ones. Computing this sensitivity matrix efficiently and accurately is far from trivial, and we can accomplish this via the use of automatic differentiation (Leal et al., 2018).

Once the predicted output $\tilde{y}$ is calculated, it must be tested for acceptance. For this, we introduce a function $g(\mathring{y}, \tilde{y}) < \varepsilon$ that assess whether $\tilde{y}$ is a sufficiently accurate approximation of the exact output $y = f(x)$ with a preselected tolerance $\varepsilon > 0$. The *acceptance test function* $g(\mathring{y}, \tilde{y})$ (which can vary across applications of the ODML algorithm) resolves to either an *acceptance* or *rejection*, and it does not require the evaluation of a computationally expensive function f. For more details on the acceptance criterion and how the reference elements are stored in priority-based clusters, we refer the reader to Leal et al. (2020).

4 Results

In this section, we investigate the performance of the *on-demand machine learning* (ODML) strategy when applied to accelerate relatively complex reactive transport simulations. A brief review of the ODML algorithm is given in Section (3.4). For more in-depth details, we refer to Leal et al. (2020) and its implementation in the open-source software Reaktoro (Leal, 2015). This section aims to demonstrate that the ODML enables faster reactive transport simulations without compromising accuracy. It is essential to mention that the ODML is mass-conservative, so all predicted chemical equilibrium states respect the mass conservation of chemical elements and electric charge.

In Leal et al. (2020), we demonstrate the algorithmic and computing features of the ODML method using relatively simple one-dimensional reactive transport simulations. Here, we consider two reactive transport problems with more complex chemical and geologic conditions in the simulations. The first problem models the dolomitization phenomenon in a rock column, similar to the one discussed in the numerical test of Leal et al. (2020). We repeat this test deliberately to enable comparing the numerical results and obtained computation speedups. The second problem addresses H_2S-scavenging of a siderite-bearing reservoir, which is particularly essential for the oil and gas industry.

Activity models and thermodynamic data. The activity coefficients of the aqueous species are calculated using the Pitzer model (Pitzer, 1973) (formulated by Harvie et al. (1984), except for the aqueous species CO_2(aq), for which the Drummond (1981) activity model is applied), the Debye-Hückel (DH) (Debye and Hückel, 1923), and the Helgeson-Kirkham-Flowers (HKF) (Helgeson and Kirkham, 1974a,b, 1976; Helgeson et al., 1981) activity models. The standard chemical potentials of the species are calculated using the equations of state of Helgeson and Kirkham (1974a); Helgeson et al. (1978); Tanger and Helgeson (1988); Shock and Helgeson (1988), and Shock et al. (1992). The model of Wagner and Pruss (2002) is chosen to compute the density of water and its temperature and pressure derivatives. Two database files are used to obtain corresponding parameters for calculations. In particular, for the dolomitization modeling discussed in Subsection 4.1, we use the `slop98.dat` database, whereas for the scavenging example in Subsection 4.2, the `slop07.dat` database is utilized. Both databases are generated by the SUPCRT92 (Johnson et al., 1992) software.

Numerical methods and other setup details. For the numerical investigations presented below, the Darcy velocity and the pressure approximations in (7) are calculated using the SDHM method (Núñez et al., 2012). Instead of updating them at each simulation step, the pair $(\boldsymbol{u}, p)$ is reconstructed only once at the beginning of the reactive transport simulation due to insignificant porosity changes. Besides, the main goal of this work is to evaluate the ODML algorithm

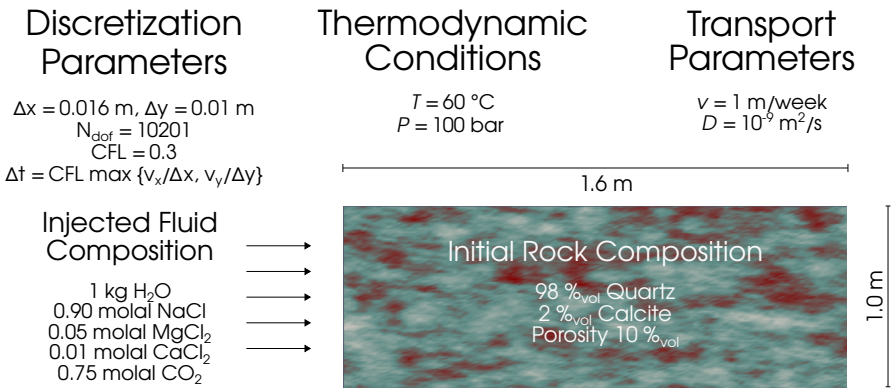


Figure 1: Illustration of the fluid injection into the two-dimensional rock core, including some details on rock composition, transport parameters, and numerical discretization.

performance under more challenging conditions. In (7), we assume zero source-term, whereas $\varrho = 1000.0$ kg/m^3 and $\mu = 8.9 \cdot 10^{-4}$ Pa $\cdot$ s. For the pressure, $p_{\text{inlet}} = P_{\text{inlet}}$ on the left side of the rock and $p_{\text{outlet}} = 0.9 P_{\text{inlet}}$ on the right boundary of the rock. The heterogeneous permeability of the rock with (preferential flow path) was obtained using the open-source Python package `GeoStatTools`(Müller and Schüler, 2019).

4.1 Case I: Reactive transport modeling of dolomitization process

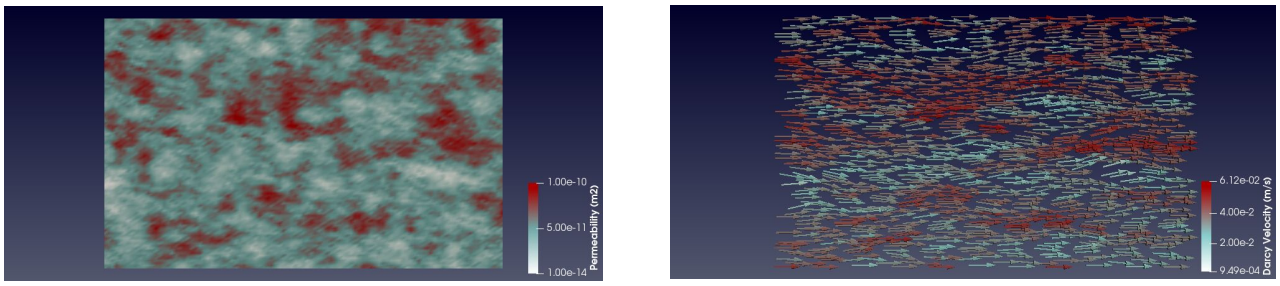
Model setup, initial and boundary conditions. The reactive transport model carried out in this section is illustrated in Figure 1. The vertical and horizontal lengths of the rock are chosen to be 1.6 m and 1.0 m, respectively. By discretizing both dimensions with 100 cells (or 101 FEM nodes), we obtain 10201 degrees of freedom (DOFs). At each DOF, we keep track of the entire chemical state of the system, i.e., its temperature, pressure, bulk concentrations of the species, and thermochemical properties (species activities, phase densities, phase enthalpies, etc.).

Initial and boundary conditions, as well as transport and thermodynamic parameters, are summarized in Table 1. For the *initial condition*, we consider the rock plate (having 10% porosity) with a mineral composition of 98%$_{\text{vol}}$ SiO_2(quartz) and 2%$_{\text{vol}}$ $CaCO_3$(calcite). The resident fluid comprises 0.70 molal NaCl brine in equilibrium with the rock minerals (with pH=9.2). The *boundary condition* is defined by an aqueous fluid injected on the left side of the rock. Its chemical composition includes 0.90 molal NaCl, 0.05 molal $MgCl_2$, 0.01 molal $CaCl_2$, and 0.75 molal CO_2 (with pH=3.1). As a result, we perform reactive transport simulation for a *chemical system* with 33 aqueous and 3 mineral species distributed among 4 phases and composed of 9 elements (presented in Table 2). First, all the calculations are performed using the HKF activity model for the aqueous species. Later in this subsection, we also apply the Pitzer model to compare the acceleration obtained for the different modeling scenarios. The temperature of the resident and injected fluids (corresponding to the initial and boundary conditions, respectively) is 60 °C. For the inlet pressure, we consider $P_{\text{inlet}} = 100$ bar. The heterogeneous permeability of the rock is presented in Figure 2a next to the pore velocity in Figure 2b reconstructed as the numerical solution of (7). The diffusion coefficient is fixed to be $D = 10^{-9}$ m^2/s for all fluid species.

Accuracy of generated chemical fields. Figure 3 compares two-dimensional chemical fields generated by the reactive transport simulation using the conventional chemical equilibrium algo-

Table 1: Summary of the parameters in the dolomitization example in Case I.

	Annotation	Description	Value
Thermodynamic Conditions	T	temperature	60 °C
	P	pressure	100 bar
Physical Properties	D	diffusion coefficient	$10^{-9}\,\mathrm{m}^2/\mathrm{s}$
Discretization Parameters	Δx	spatial mesh-size along the x-axis	1.6 cm (0.016 m)
	Δy	spatial mesh-size along the y-axis	1.0 cm (0.01 m)
	$\mathrm{N_{dofs}}$	number of degrees of freedom	10201
	Δt	temporal discretization step	$\Delta t = \mathrm{CFL}/\max\left\{\max\lvert v_x\rvert/\Delta x, \max\lvert v_y\rvert/\Delta y\right\}$
Initial Condition, pH = 9.2	ϕ	porosity *(not kept constant)*	10%
	Rock composition		
	SiO_2	quartz	$98\%_{\mathrm{vol}}$
	$CaCO_3$	calcite	$2\%_{\mathrm{vol}}$
	Resident fluid composition (NaCl-brine)		
	NaCl	sodium chloride	0.70 molal
Boundary Condition, pH = 3.05	*Injected fluid composition* (NaCl-$MgCl_2$-$CaCl_2$-brine saturated with CO_2)		
	NaCl	sodium chloride	0.90 molal
	$MgCl_2$	magnesium chloride	0.05 molal
	$CaCl_2$	calcium chloride	0.01 molal
	CO_2	carbon dioxide	0.75 molal



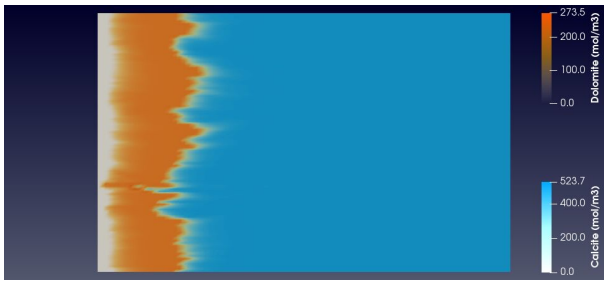
(a) (b)

Figure 2: (a) The permeability field and (b) the pore velocity field in the dolomitization example.

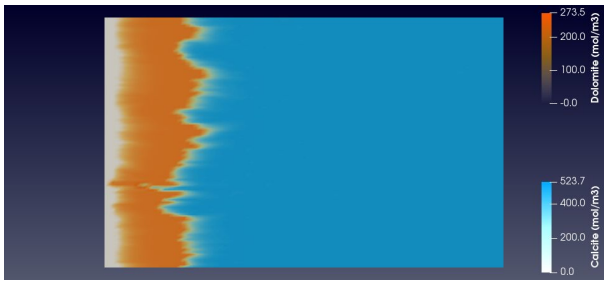
Table 2: Description of the chemical system used in the dolomitization example.

Elements	C, Ca, Cl, H, Mg, Na, O, Si, Z*						
Phases	Aqueous, Calcite, Dolomite, Quartz						
Species	$CO_2(aq)$	$CaCl^+(aq)$	$ClO_2^-(aq)$	$H_2O(l)$	$HClO_2(aq)$	$MgCl^+(aq)$	$O_2(aq)$
	$CO_3^{2-}(aq)$	$CaCl_2(aq)$	$ClO_3^-(aq)$	$H_2O_2(aq)$	$HO_2^-(aq)$	$MgOH^+(aq)$	$OH^-(aq)$
	$Ca(HCO_3)^+(aq)$	$CaOH^+(aq)$	$ClO_4^-(aq)$	$HCO_3^-(aq)$	$Mg(HCO_3)^+(aq)$	$Na^+(aq)$	$CaCO_3$ (calcite)
	$Ca^{2+}(aq)$	$Cl^-(aq)$	$H^+(aq)$	$HCl(aq)$	$Mg^{2+}(aq)$	$NaCl(aq)$	$CaMg(CO_3)_2$ (dolomite)
	$CaCO_3(aq)$	$ClO^-(aq)$	$H_2(aq)$	$HClO(aq)$	$MgCO_3(aq)$	$NaOH(aq)$	SiO_2 (quartz)

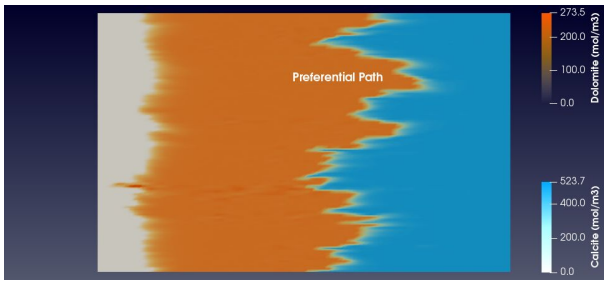
* Z is the symbol for the element representing an electric charge.



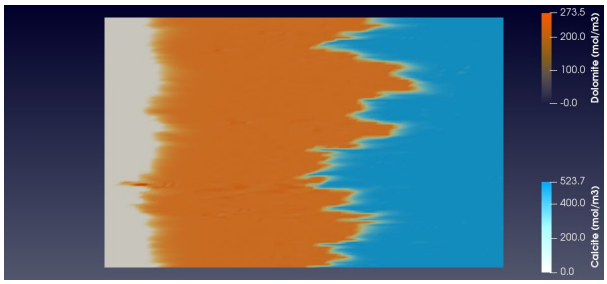
(a) step 500 with the conventional algorithm



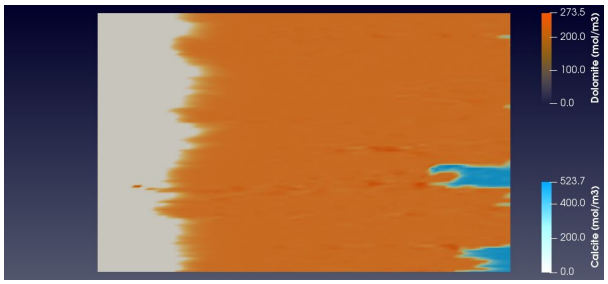
(b) step 500 with the ODML algorithm



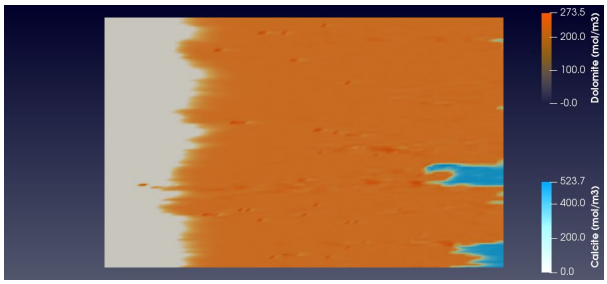
(c) step 1500 with the conventional algorithm



(d) step 1500 with the ODML algorithm

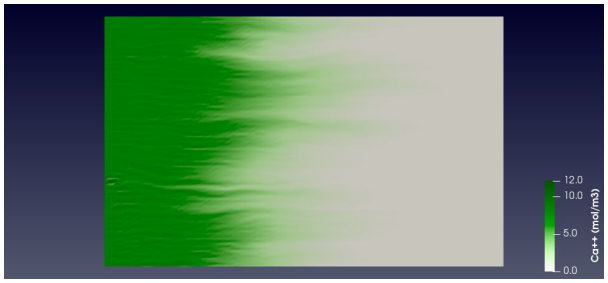


(e) step 2500 with the conventional algorithm

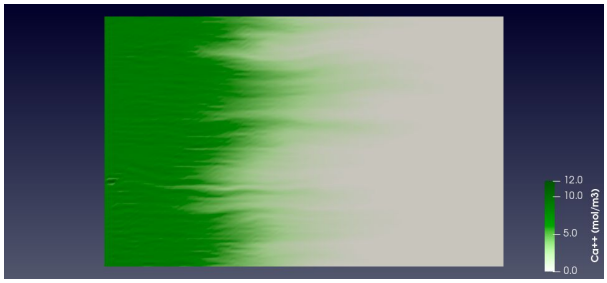


(f) step 2500 with the ODML algorithm

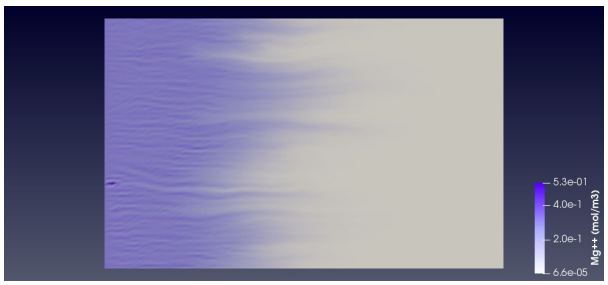
Figure 3: The amount of minerals calcite and dolomite (in mol/m^3) in the two-dimensional rock core at time steps 500, 1500, and 2500, which correspond to 0.48, 1.43, and 2.38 days of simulations. The plots *on the left* are results of the *benchmark reactive transport simulation* where chemical calculations are carried out by conventional chemical equilibrium calculations based on ***full GEM calculations*** performed in every cell of each time step. The plots *on the right* are the chemical fields generated during the same simulation but ***applying the ODML algorithm*** with $\varepsilon = 0.001$.



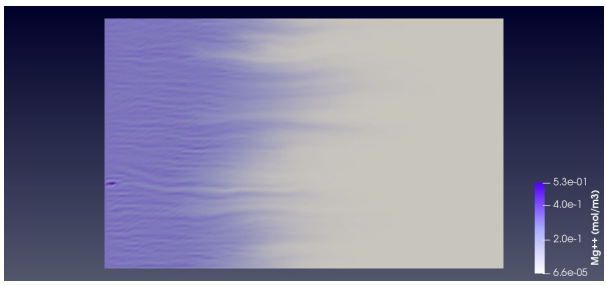
(a) Ca^{2+} with the conventional algorithm



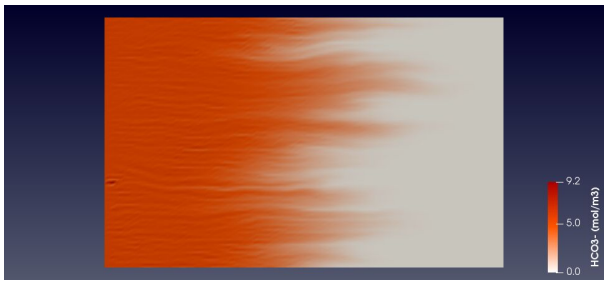
(b) Ca^{2+} with the ODML algorithm



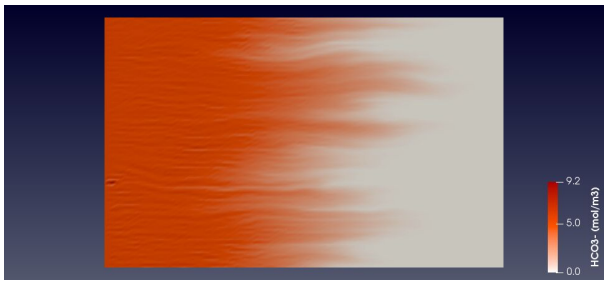
(c) Mg^{2+} with the conventional algorithm



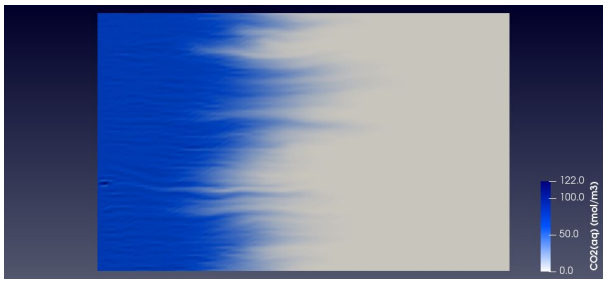
(d) Mg^{2+} with the ODML algorithm



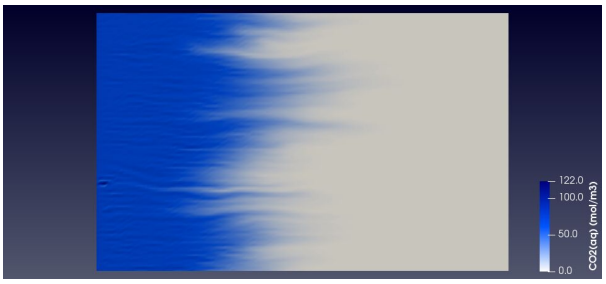
(e) HCO_3^- with the conventional algorithm



(f) HCO_3^- with the ODML algorithm

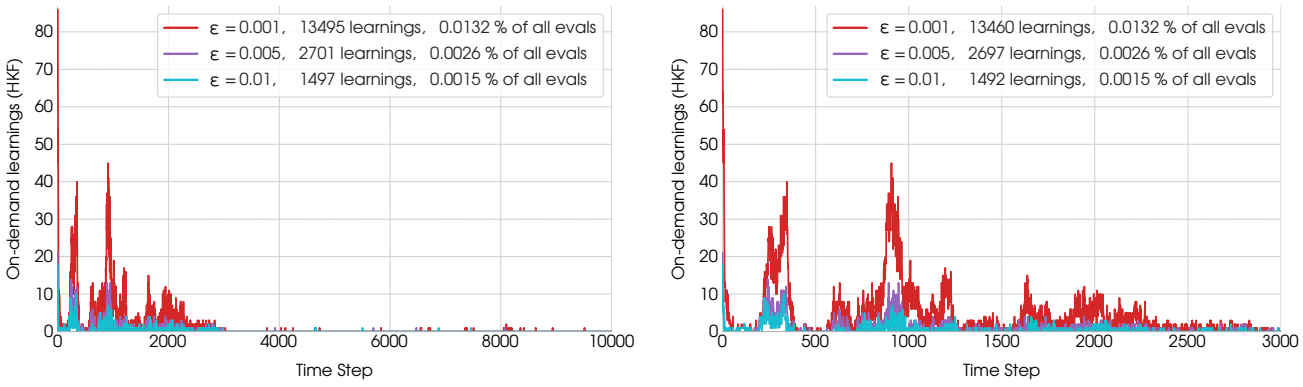


(g) CO_2(aq) with the conventional algorithm



(h) CO_2(aq) with the ODML algorithm

Figure 4: The amount of selected aqueous species (in molal) in the two-dimensional rock core at time step 20, corresponding to 27.42 minutes of simulations. The plots *on the left* are the results of *the benchmark reactive transport simulation* where chemical calculations are carried out by conventional chemical equilibrium calculations based on full GEM calculations performed in every cell of each time step. The plots *on the right* are the chemical fields generated during the same simulation but *applying the ODML algorithm* with $\varepsilon = 0.001$.

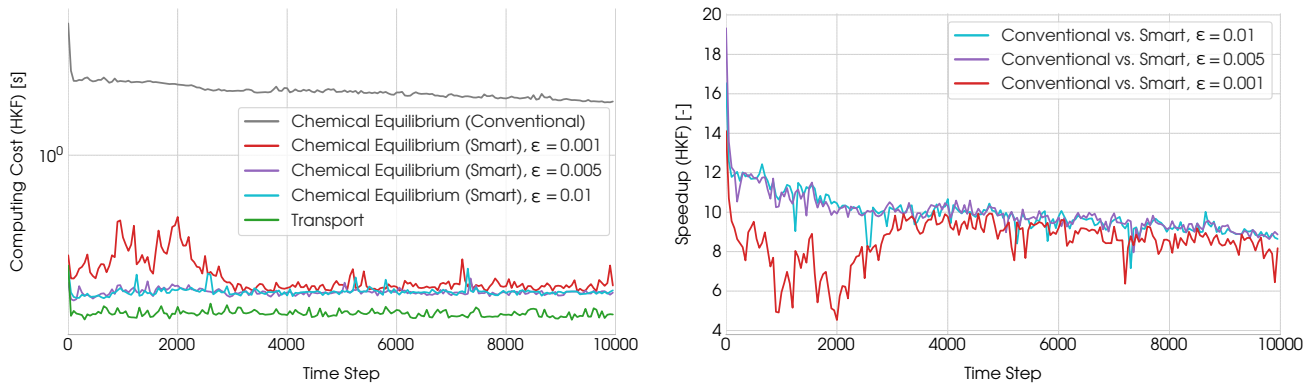


(a) (b)

Figure 5: (a) The number of *on-demand learning operations* triggered by the ODML algorithm at each time step (illustrated for different values for the acceptance tolerance ε). Each learning operation requires the full solution of the non-linear equations governing chemical equilibrium using a Newton-based numerical method. We run simulations for 10,000 time steps, with each step requiring the solution of 10,201 chemical equilibrium problems. The entire simulation thus requires a total of 102,010,000 chemical equilibrium states to be computed. The legend depicts the *total number* of *on-demand learning operations* triggered by the ODML algorithm and the percentage it accounts from the total chemical evaluations for each ε. (b) The number of *on-demand learning operations* triggered by the ODML algorithm on the first 3,000 time steps.

rithm based on the Gibbs energy minimization (on the left) and results generated by the ODML algorithm (on the right). In particular, it shows the time steps 500, 1500, and 2500 (corresponding to 0.48, 1.43, and 2.38 days of simulations) with the amounts of minerals $CaCO_3$ (calcite) and $CaMg(CO_3)_2$ (dolomite). As $CaCO_3$ dissolves, it releases Ca^{2+}(aq) ions, which react with the incoming Mg^{2+}(aq) and local carbonate and bicarbonate ions to precipitate $CaMg(CO_3)_2$. After 500 time steps of injecting the brine, we observe the dissolution of calcite (in blue) and simultaneous precipitation of dolomite (in orange). Here, some parts of the rock have pure quartz (in gray), where dolomite is gradually dissolved away as a result of the continuous injection of the acidic brine. Figures 3c and 3d, corresponding to 1500 time steps of simulations, illustrate the fields with a preferential path forming in the parts of the rock with higher permeability and, as a result, larger amplitude velocities. Finally, after 2.38 days, almost all calcite is being replaced by dolomite (see Figures 3e and 3f). The fields generated by the ODML approach (on the right) are rather close to those on the left, demonstrating high accuracy of the method even then applied to heterogeneous rocks.

Figure 4 illustrates the behavior of aqueous species Ca^{2+}(aq), Mg^{2+}(aq), HCO_3^-(aq), and CO_2(aq) after 27.42 minutes of simulations (or 20 time steps). We observe the local increase in all species concentrations as the result of the NaCl-$MgCl_2$-$CaCl_2$-brine injection. Reconstruction of the chemical fields for the aqueous species by the ODML algorithm (on the right) practically coincides with the benchmark snapshots (on the left), confirming that the smart chemical equilibrium algorithm (ODML+GEM) *does not* compromise accuracy during the simulation. These chemical fields correspond to the reactive transport simulations using the ODML acceleration strategy with tolerance $\varepsilon = 0.001$. The relative error obtained during the latter simulation is illustrated in Figure 18 in Appendix C. The confirmation on the *elemental mass conservation constraint satisfaction* for each



(a) CPU computing costs

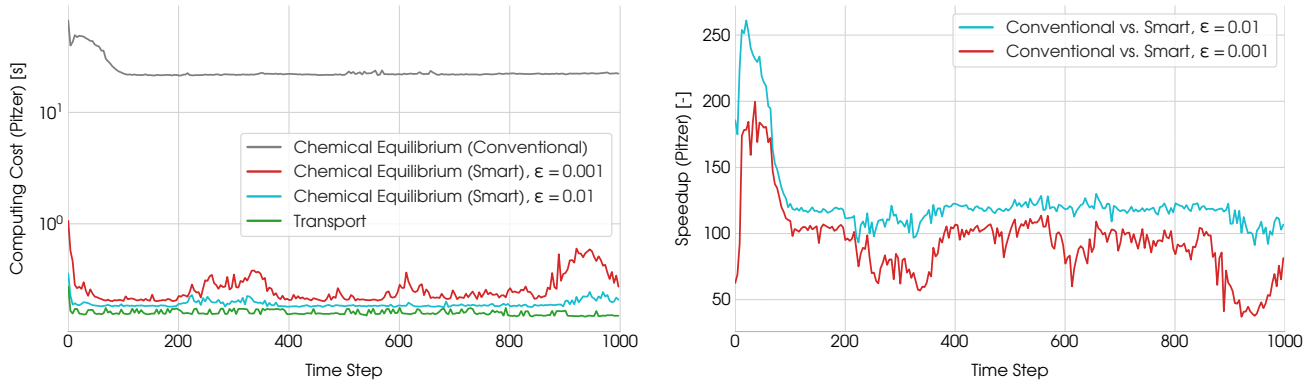
(b) speedups

Figure 6: (a) Comparison of the computing costs (CPU time in seconds) of transport, conventional, and smart chemical equilibrium calculations (run with different error control parameter ε) during each step of the reactive transport simulation. The cost of equilibrium calculations per time step is calculated as the sum of the individual costs in each discretized points, whereas the cost of transport calculations per time step is the time required when solving the discretized algebraic transport equations. (b) The speedup factor of chemical equilibrium calculations, at each time step of the simulation, resulting from the use of the on-demand learning acceleration strategy (run with different ε). For these calculations, the HKF activity model for the aqueous species was used.

element is presented in Figure 19 in Appendix C. We see that the mass balance relative error does not exceed the order of 10^{-13} and lower depending on the element.

Number of on-demand learning operations. Injecting the reactive fluid on the left part of the rock core boundary causes continual reactions in the resident fluid and rock minerals. Figure 5a illustrates the *number of triggered on-demand learnings* on each time step. Here, we select different error control parameter ε to study how they affect the number of full GEM calculations (i.e., the on-demand learning operations) required for the ODML algorithm to satisfy each such tolerance. Most of the triggered learnings happen in the first 3,000 time steps (see Figure 5b). After this, only 1-2 nodes (out of 10,201 nodes in the mesh) require occasional full and expensive chemical equilibrium calculations to guarantee imposed accuracy levels on the chemical equilibrium states and permit further subsequent states to be accurately predicted. Even though these chemical states still contain precipitating dolomite and dissolving calcite, the ODML algorithm can successfully estimate them with insignificant errors.

The legend of Figure 5a includes the number of *total trainings* required during the reactive transport simulation with the ODML algorithm having different accuracy requirements. Even though the number of trainings is ten times higher for the $\varepsilon = 0.001$ than for $\varepsilon = 0.01$, the percentage of all the learnings remains below 0.02%. Figure 5b considers only the first 3,000 time steps to magnify the difference between the number of triggered conventional evaluations for each ε. We see that the total number of learnings triggered on these time steps for $\varepsilon = 0.001$, for instance, is 99.73% (13460 out of 13496) of all needed full evaluations. We note that unlike homogeneous one-dimensional numerical test considered in (Leal et al., 2020), where on-demand learnings were the highest on the first few times step and then gradually decayed as reactive transport proceeds, in the heterogeneous case, we see several spikes in the number of learnings. See, for example,



(a) CPU computing costs

(b) speedups

Figure 7: (a) Comparison of the computing costs (CPU time in seconds) of transport, conventional, and smart chemical equilibrium calculations during each time step of the reactive transport simulation for different ε. The cost of equilibrium calculations per time step is calculated as the sum of the individual costs in each degree of freedom, whereas the cost of transport calculations per time step is the time required when solving the discretized algebraic transport equations. (b) The speedup factor of chemical equilibrium calculations, at each time step of the simulation, resulting from the use of the on-demand learning acceleration strategy with different ε. All the calculations are performed using the HKF activity model for the aqueous species.

the increase in the number of learnings between steps 250 and 350, or between 850 and 1000. Such a sudden increase can be explained by the dissolution and precipitation front of the chemical system reaching different parts of the rock with increasing/decreasing permeabilities and corresponding to more significant or lower amplitudes of the velocity. Having said that, the percentage of the total number of fast and accurate chemical equilibrium predictions enabled by the ODML algorithm remains higher than ~99.9% of all chemical equilibrium problems required in the simulations (i.e., less than ~0.1% of all such problems are actually solved using a full and expensive chemical equilibrium calculation provided by a conventional GEM or LMA algorithm).

Computing cost reduction using ODML (when HKF activity model is used). Figure 6a compares the computational cost (measured as CPU time in seconds) of *(i)* conventional chemical equilibrium calculations, *(ii)* smart chemical equilibrium calculations, and *(iii)* transport calculations at each time step. These simulation runs are performed for different ε assigned to the ODML algorithm. For the transport calculations, the cost comprises of the time needed to solve the linear systems algebraic transport equations generated by the SUPG method. The figure highlights that the CPU cost of conventional chemical equilibrium calculations is 1-2 orders of magnitude higher than the cost of transport calculations. We see that the computational cost associated with chemical equilibrium calculations can be substantially reduced using the ODML approach. Smaller the predefined error control tolerance ε is, higher the number of on-demand learning (full GEM calculation) is. This also affects the CPU time of the corresponding ODML simulation (especially on the first 3000 steps).

Figure 6b presents the speedup of the ODML algorithm that is calculated at each reactive transport simulation step as a ratio of the accumulated time needed for the conventional and smart chemical equilibrium calculations across all cells in the mesh. All three depicted speedups correspond to the CPU costs and tolerances considered in Figure 6a. The red curve illustrates the

Table 3: Clusters created by the ODML algorithm ($\varepsilon = 0.01$) during the reactive transport simulation of a chemical system with 33 aqueous species using the HKF activity model. *Clusters* # reflects the order they were created. *Frequency* / *Rank* is the number of times the cluster was used to retrieve suitable reference equilibrium state for new prediction. Column *Records* lists the number of fully calculated and stored chemical equilibrium states in the cluster. This statistical information indicates that two clusters, #21 and #28, with relatively few numbers of recorded fully computed chemical equilibrium states, 1 and 3, respectively, are responsible for the majority of smart and fast estimation in total equilibrium evaluations. In particular, clusters #21 and #28 are responsible for 48,09% and 27.93 %, respectively, of all 102,010,000 fast predictions, and together, these two clusters only have 4 learned equilibrium calculations.

Clusters #	**Primal Species**	**Frequency / Rank**	**# of Records**
1	H_2O(l) Calcite Cl^- Na^+ CO_2(aq) Ca^{2+} Dolomite O_2	1,799,389	2
2	H_2O(l) Calcite Cl^- Na^+ HCO_3^- Ca^{2+} Dolomite O_2	326	1
3	H_2O(l) Calcite Cl^- Na^+ HCO_3^- Ca^{2+} Mg^{2+} O_2	54,553	15
4	H_2O(l) Calcite Cl^- Na^+ Ca^{2+} HCO_3^- Mg^{2+} O_2	118,099	1
5	H_2O(l) Calcite Na^+ Cl^- OH^- H_2(aq) Ca^{2+} Mg^{2+}	0	7
6	H_2O(l) Calcite Na^+ Cl^- H_2(aq) OH^- Ca^{2+} Mg^{2+}	0	3
7	H_2O(l) Calcite Na^+ Cl^- OH^- Ca^{2+} H_2(aq) Mg^{2+}	0	1
8	H_2O(l) Calcite Cl^- Na^+ OH^- Ca^{2+} H_2(aq) Mg^{2+}	0	11
9	H_2O(l) Calcite Cl^- $Na^+$$Ca^{2+}$ OH^- O_2 Mg^{2+}	5	7
10	H_2O(l) Calcite Cl^- Na^+ Ca^{2+} $OH^-$$H_2$(aq) Mg^{2+}	0	1
11	H_2O(l) Calcite Cl^- $Na^+$$Ca^{2+}$$HCO_3^-$ O_2 Mg^{2+}	19	2
12	H_2O(l) Calcite Cl^- Na^+ CO_2(aq) Ca^{2+} Mg^{2+} O_2(aq)	10,914,505	8
13	H_2O(l) Calcite Cl^- Na^+ HCO_3^- Ca^{2+} H_2(aq) Mg^{2+}	0	1
14	H_2O(l) Calcite Cl^- Na^+ CO_2(aq) Ca^{2+} H_2(aq) Mg^{2+}	1,448	23
15	H_2O(l) Calcite Cl^- Na^+ OH^- Ca^{2+} Dolomite O_2(aq)	1	1
16	H_2O(l) Calcite $Na^+$$Cl^-$ H_2(aq) OH^- Ca^{2+} Dolomite	0	2
17	H_2O(l) Calcite Cl^- Na^+ OH^- Ca^{2+} O_2(aq) Mg^{2+}	1	3
18	H_2O(l) Calcite Cl^- Na^+ OH^- Ca^{2+} Mg^{2+} O_2	3	3
19	H_2O(l) Calcite Cl^- Na^+ Ca^{2+} $OH^-$$Mg^{2+}$ O_2	2	1
20	H_2O(l) Dolomite Cl^- Na^+ CO_2(aq) Ca^{2+} HCO_3^- O_2(aq)	7,910	1
21	H_2O(l) Dolomite Cl^- Na^+ CO_2(aq) Mg^{2+} Ca^{2+} O_2(aq)	49,064,564	1
22	H_2O(l) Dolomite Cl^- Na^+ CO_2(aq) Ca^{2+} Mg^{2+} O_2(aq)	3,436	1
23	H_2O(l) Calcite Cl^- Na^+ CO_2(aq) Ca^{2+} H_2(aq) Dolomite	123,437	1,225
24	H_2O(l) Cl^- Na^+ CO_2(aq) Mg^{2+} HCO_3^- Ca^{2+} O_2(aq)	77,608	2
25	H_2O(l) Cl^- Na^+ CO_2(aq) Mg^{2+} Ca^{2+} H^+ O_2(aq)	11,283,955	32
26	H_2O(l) Dolomite Cl^- Na^+ CO_2(aq) Mg^{2+} HCO_3^- H_2(aq)	4	27
27	H_2O(l) Calcite Cl^- Na^+ CO_2(aq) Ca^{2+} O_2(aq) Dolomite	66	18
28	H_2O(l) Cl^- Na^+ CO_2(aq) Mg^{2+} Ca^{2+} HCO_3^- O_2(aq)	28,499,792	3
29	H_2O(l) Cl^- Na^+ CO_2(aq) Mg^{2+} H^+ Ca^{2+} O_2(aq)	64,339	13
30	H_2O(l) Calcite Cl^- Na^+ CO_2(aq) Dolomite Ca^{2+} H_2(aq)	8	16
31	H_2O(l) Calcite Dolomite Cl^- Na^+ CO_2(aq) Ca^{2+} H_2(aq)	15	44
32	H_2O(l) Calcite Cl^- Dolomite Na^+ CO_2(aq) Ca^{2+} H_2(aq)	18	15
33	H_2O(l) Calcite Cl^- Na^+ Dolomite CO_2(aq) Ca^{2+} H_2(aq)	0	6

speedup achieved by the ODML algorithm with the strictest ε, and, as expected, it reaches the lowest speedup values until the time step 3000. The blue and purple curves depicting the speedups of the ODML algorithm performed with tolerances $\varepsilon = 0.01$ and $\varepsilon = 0.005$, respectively, indicate a similar acceleration level. We highlight that all the lines converge to the same speedup approximate to 9x. Such behavior only confirms that no matter how many reference chemical states are collected during the on-demand learning operations by the ODML algorithm, the search algorithm, employing the priority-based clustering (presented in (Leal et al., 2020)), does not affect the CPU costs on the later time steps of the reactive transport.

Computing cost reduction using ODML (when Pitzer activity model is used). Besides the HKF activity model, we have run simulations using the Pitzer activity models. From Figure 7 (illustrated only for 1000 time steps, 10% of all reactive transport steps), we see that the CPU time of the chemical equilibrium computations and corresponding speedups strongly depend on the activity model applied. Generally, the Pitzer model is considerably more expensive to evaluate and require more Newton iterations to minimize Gibbs energy, compared to the HKF model. Performed simulation results in a way higher speedups, which can be achieved with the ODML algorithm. Depicting two different scenarios, $\varepsilon = 0.01$ and $\varepsilon = 0.001$, Figure 7b confirms that for simulations with the Pitzer model, the ODML algorithm might result in 10 times higher speedups than for the HKF model. The recap of the overall number of learnings, the percentage of the smart predictions with respect to the number of total chemical equilibrium calculations, the lowest and highest speedups in chemical equilibrium calculations throughout the time steps, as well as the overall speedups in the reactive transport simulations achieved by the ODML method for different tolerances and activity models are summarized in Figure 17a.

Clustering during the simulation process. During the reactive transport simulation, we use the on-demand clustering strategy introduced in Leal et al. (2020). This strategy classifies chemical states based on their associated *primary species*. The set of clusters is updated every time the on-demand learning operation happens. During such learning/training, a new fully evaluated chemical equilibrium state is produced (with a zero priority rank) and stored. If the primary species of this chemical state coincide with the primary species in one of the existing clusters, this particular cluster will be enriched with a newly learned reference state. If we fully compute a new chemical equilibrium state and no clusters correspond to the primary species in that state, a new cluster is created to store it. Whenever a reference chemical equilibrium state is successfully used to predict another, its *priority rank* (and also the priority rank of the cluster where it is stored) is incremented. Within each cluster, the records of learned chemical equilibrium states are sorted so that those with higher success rates/ranks are used first.

Table 3 lists all clusters created during the simulation, along with their associated primary species. The first column reflects the order (in time), in which the ODML method generated them in the course of the numerical experiment. Besides primary species, the table shows how often each cluster was a successful provider of a reference equilibrium state for Taylor extrapolation (third column) and how many learned equilibrium states each cluster stores (fourth column). For instance, Calcite is stable in the majority of clusters, i.e., Clusters 1–19, 23, 27, 30-33, but unstable in some of the clusters created on later times, reflecting the equilibrium states in which this mineral becomes wholly dissolved. Clusters 20–22, 26 are responsible for chemical states where dolomite is stable or precipitates. Its different position in primary species of Clusters 1-2, 15-16, 23, 27, 30-33 indicates that the mineral is either available in more significant or minor abundance in corresponding mesh cells. Equilibrium states, in which both minerals are entirely dissolved in the simulation, are represented by Clusters 24-25 and 28-29. It is highly probable that these clus-

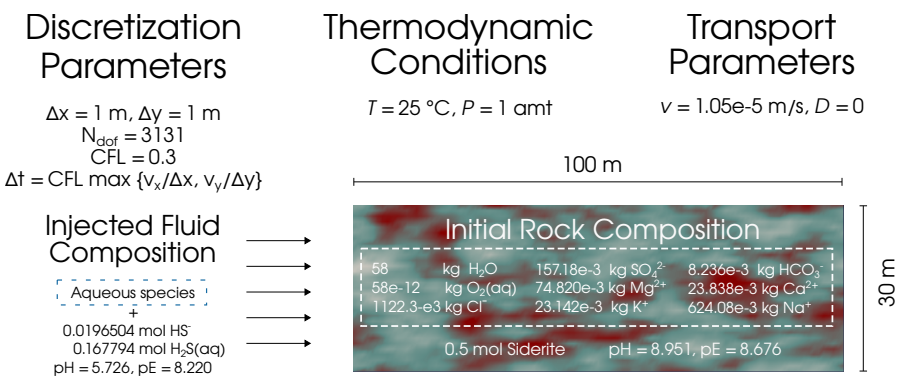


Figure 8: Illustration of the injection fluid into the two-dimensional siderite bearing reservoir, including some details on rock composition, transport parameters, and numerical discretization in the H_2S-scavenging example.

ters could be used more frequently if the simulations continued for a much longer time since they represent equilibrium states without carbonate minerals but with pore fluid composition identical to the injected fluid. Cluster 21 has the highest rank in providing suitable reference equilibrium states for accurate approximations of the ODML algorithm. A single reference equilibrium state of this cluster was successfully used **49,064,564 times for predictions**, which accounts for 48.06% of all chemical equilibrium evaluations.

4.2 Case II: Reactive transport modeling of H_2S scavenging

We now consider a reactive transport modeling of sulfide scavenger, a widely adopted practice in the production and processing operations in the oil and gas industry. By *sulfide scavenger,* we mean any chemical that can react with one or more sulfide species (H_2S, HS^-, and S_2^-, ect.) and convert them to a more inert form. For that purpose, siderite ($FeCO_3$) is considered below. Generally, the increase of the hydrogen sulfide mass in produced fluids due to activities of sulfate-reducing bacteria (SRB) as a result of water-flood is referred to as *the reservoir souring*. The field level prediction of the H_2S generation and production is a significant phenomenon to model due to several following reasons. Hydrogen sulfide is not only highly toxic for humans and animals, but is extremely corrosive to most metals involved in the field operations. It may cause cracking of drill or transport pipes and tubular goods, and destroy the testing tools and wire lines. Therefore, the reactive transport modeling of the mineral-H_2S reactions is essential for studying the field-specific hydrogen sulfide scavenging capacities.

Model setup, initial and boundary conditions. Similar to the previous example, Figure 8 shows the reactive transport modeling carried out in this subsection. For the reservoir, the horizontal and vertical lengths are 100 and 30 meters. We consider 100 and 30 cells (or 101 and 31 DOFs) for its discretization, which results in a total of 3131 DOFs that must be considered in each time step. We fix the temperature to 25 °C and inlet pressure to 1 atm (1.01325 bar), respectively . The heterogeneous permeability is illustrated in Figure 9a, whereas the corresponding velocity $\boldsymbol{v}$ is shown in Figure 9b. The diffusion of fluid species is neglected. The resident fluid in the siderite-bearing ($FeCO_3$) reservoir, the content of the injected brine, and transport and thermodynamic parameters are summarized in Table 4. The considered system contains 77 aqueous

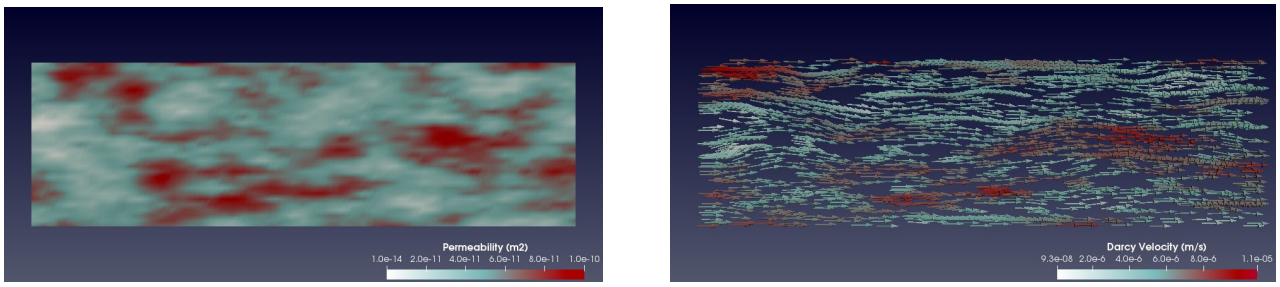
Table 4: Summary of the parameters for the H_2S-scavenging example.

	Annotation	Description	Value
Thermodynamic Conditions	T	temperature	25 °C
	P	pressure	1 atm = 1.01325 bar
Physical Properties	$\boldsymbol{v}$	fluid pore velocity	$1.05 \cdot 10^{-5}$ m/s
	D	diffusion coefficient	$0\,\mathrm{m}^2/\mathrm{s}$
Discretization Parameters	Δx	spatial mesh-size along the x-axis	1.0 m
	Δy	spatial mesh-size along the y-axis	1.0 m
	N_{dofs}	number of degrees of freedom	3131
	Δt	temporal discretization step	$\Delta t = \mathrm{CFL}/\max\left\{\max\lvert v_x\rvert/\Delta x, \max\lvert v_y\rvert/\Delta y\right\}$
Initial Condition, pH = 8.951, pE = 8.676	ϕ	Porosity *(not kept constant)*	10%
	Rock composition		
	$FeCO_3$	siderite	0.5 mol
	Resident fluid composition		
	H_2O	water	58 kg
	O_2(aq)	oxygen	58e-9 g
	Cl^-	chlorine anion	1122.3 g
	SO_4^{2-}	sulphate ion	157.18 g
	Mg^{2+}	magnesium cation	74.820 g
	HCO_3^-	carbonate anion	8.236 g
	Ca^{2+}	calcium cation	23.838 g
	Na^+	sodium cation	624.08 g
	K^+	potassium cation	23.142 g
Boundary Condition, pH = 5.726, pE = 8.220	*Injected fluid composition* (H_2S-brine)		
	Resident fluid composition +		
	H_2S(aq)	hydrogen sulfide	0.167794 molal
	HS^-	hydrogen sulfide anion	0.0196504 molal

Table 5: Description of the chemical system used in the H_2S-scavenging example.

Elements	C, Ca, Cl, Fe, H, K, Mg, Na, O, Si, Z*							
Phases	Aqueous, Siderite, Pyrrhotite							
Species	CO(aq)	$CaSO_4$(aq)	$FeCl^{2+}$	H_2O(l)	$HFeO_2$(aq)	K^+	$MgOH^+$	$S_2O_3^{2-}$
	CO_2(aq)	Cl^-(aq)	$FeCl_2$(aq)	H_2O_2(aq)	$HFeO_2^-$	KCl(aq)	$MgSO_4$(aq)	$S_2O_4^{2-}$
	CO_3^{2-}(aq)	ClO^-(aq)	FeO (aq)	H_2S(aq)	HO_2^-	$KHSO_4$(aq)	Na^+	Siderite
	$Ca(HCO3)^+$(aq)	ClO_2^-(aq)	FeO^+	$H_2S_2O_3$(aq)	HS^-	KHO (aq)	NaCl(aq)	Pyrrhotite
	Ca^{2+}(aq)	ClO_3^-(aq)	FeO_2^-	$H_2S_2O_4$(aq)	$HS_2O_3^-$	KSO_4^-	NaOH(aq)	
	$CaCO_3$(aq)	ClO_4^-(aq)	$FeOH^+$	HCO_3^-(aq)	$HS_2O_4^-$	$Mg(HCO3)^+$	$NaSO_4^-$	
	$CaCl^+$(aq)	Fe^{2+}	$FeOH^{2+}$	HCl(aq)	HSO_3^-	Mg^{2+}	O_2(aq)	
	$CaCl_2$(aq)	Fe^{3+}	H^+	HClO(aq)	HSO_4^-	$MgCO_3$(aq)	OH^-(aq)	
	$CaOH^+$(aq)	$FeCl^+$	H_2(aq)	$HClO_2$(aq)	HSO_5^-	$MgCl^+$	S_2^{2-}	

* Z is the symbol for the element representing an electric charge.



(a) (b)

Figure 9: (a) The permeability field and (b) the pore velocity in the H_2S-scavenging example.

and 2 mineral species distributed among 3 phases and composed of 10 distinct elements (see Table 5). We acknowledge that in the ideal reservoir simulations, the rock matrix must contain the different proportion of minerals such as quartz, calcite, etc. However, such a simplification is assumed for the purpose of studying the scavenging process solely.

As highlighted above, the numerical test conducted in this section considers heterogeneous siderite-bearing reservoir continuously perturbed by the H_2S-rich brine on the left side of the boundary. Being highly soluble, siderite ($FeCO_3$) reacts with H_2O, HS^-, H_2S species in the injected fluid and dissolves donating the iron ion Fe^{2+}, i.e.,

$$FeCO_3 \rightleftharpoons Fe^{2+} + CO_3^{2-}.$$

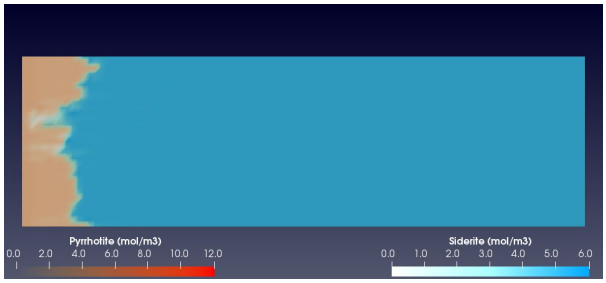
At the same time, the donated iron ions react with the sulfides (delivered by the brine) such that iron-sulfide FeS (also known as pyrrhotite) starts to precipitate:

$$HS^- + Fe^{2+} \rightleftharpoons FeS + H^+.$$

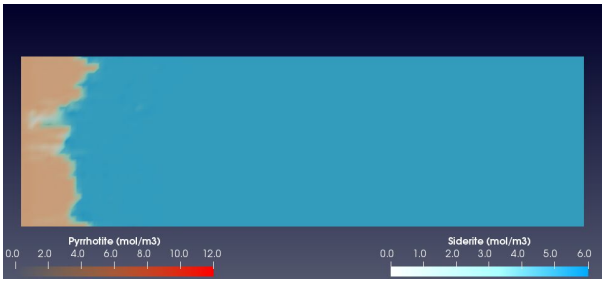
Accuracy of generated chemical fields. The dissolution of $FeCO_3$ (siderite) and precipitation of FeS (pyrrhotite) are shown in Figure 10. On the left side, we list the chemical fields generated by the reactive transport simulations using the conventional chemical equilibrium solvers. We also highlight the parts of the rock with a preferential path formed due to higher permeability. The two-dimensional chemical fields on the right side correspond to the similar simulation performed using the ODML algorithm with $\varepsilon = 0.01$. Even for such a relaxed tolerance, the behavior between siderite and pyrrhotite is rather accurately approximated using ODML.

The dissolution and precipitation of minerals are accompanied by the increase and decrease in the aqueous species concentrations. For instance, Figure 11 shows the iron ions behavior at the same steps as the siderite and pyrrhotite two-dimensional chemical fields discussed above. Throughout all the plots, we see an initial gradual increase of Fe^{2+} as a result of $FeCO_3$ dissolution. It is followed by the sharp drop of the iron ion concentration at the point of the phase transformation from one mineral to another as it gets used by the FeS formation. The width of the region, where Fe^{2+} is increased, is also getting more significant as the reactive transport simulation proceeds.

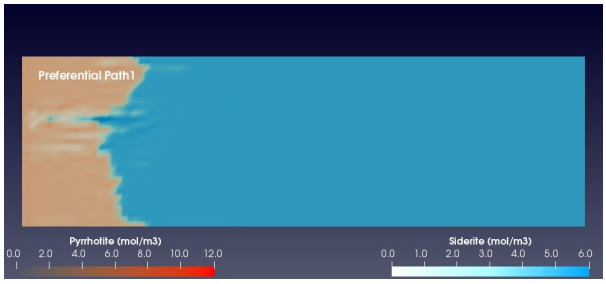
Figure 12 compares two-dimensional time snapshots of the sulfides S_2^{2-}, HS^-, and H_2S (aq) at the time step 400, which illustrates the state of the reactive transport simulations after 141.04 days. The profiles with the sharp drop of all three species amounts coincide with those parts of the rock, which injected brine has not reached yet. This profile also corresponds to the transformation



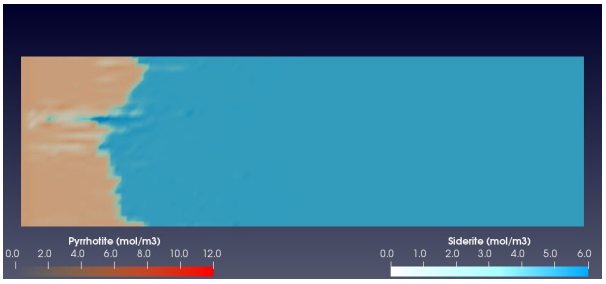
(a) step 100 with the conventional approach



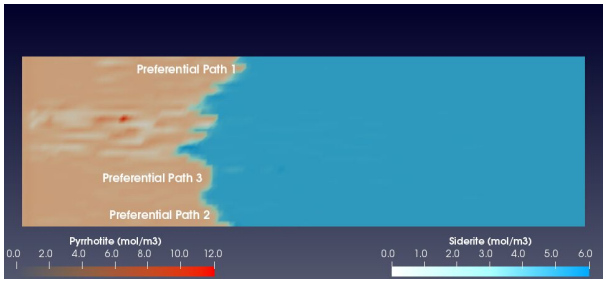
(b) step 100 with the ODML approach



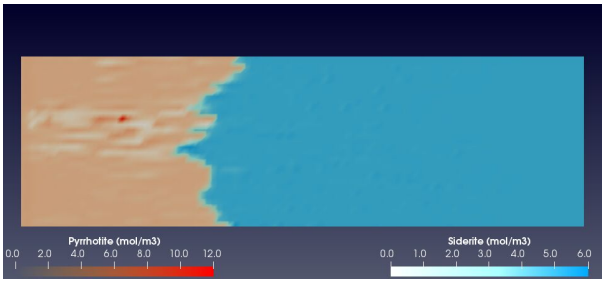
(c) step 200 with the conventional approach



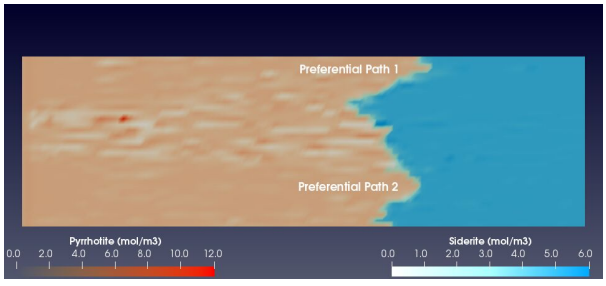
(d) step 200 with the ODML approach



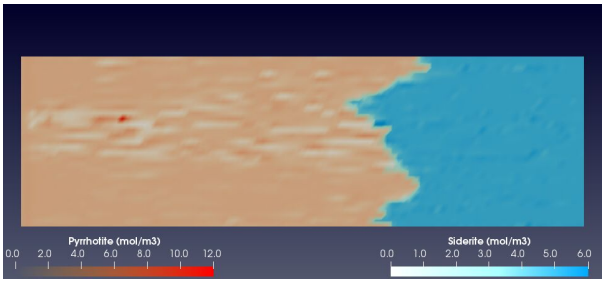
(e) step 400 with the conventional approach



(f) step 400 with with the ODML approach

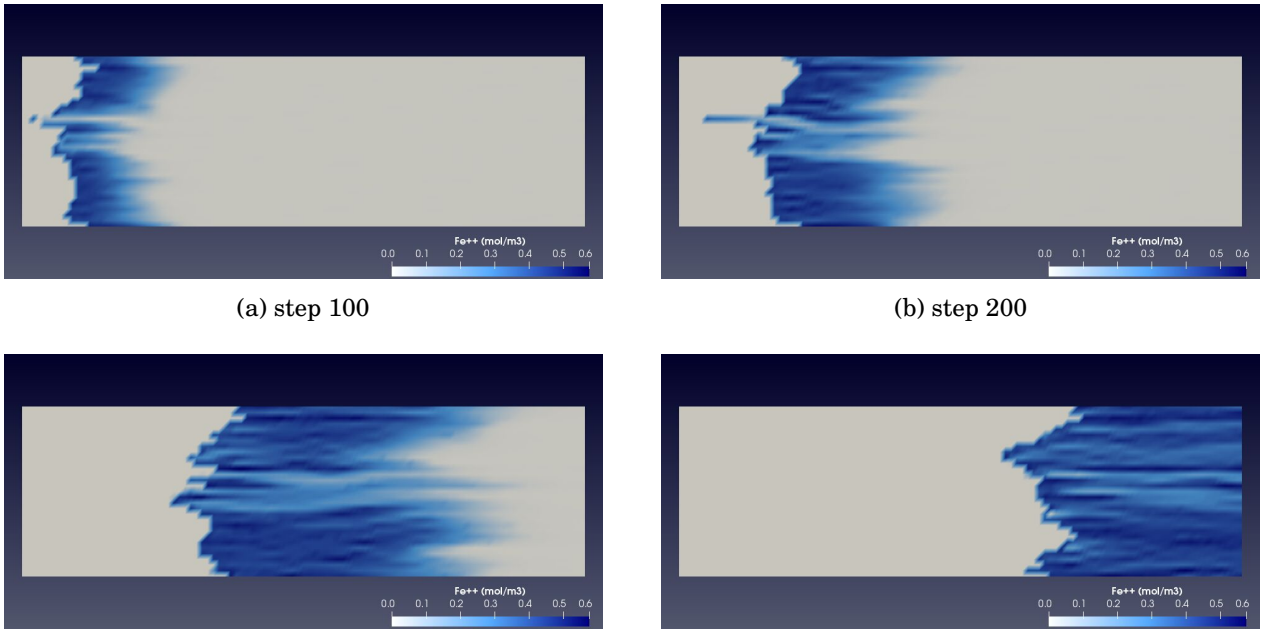


(g) step 800 with the conventional approach



(h) step 800 with the ODML approach

Figure 10: The amount of minerals siderite and pyrrhotite (in mol/m^3) in the two-dimensional rock core at time steps 100, 200, 400, and 800, corresponding to 35.26, 70.52, 141.04, and 282.08 days of simulations, respectively. The chemical fields *on the left* are generated during *the (benchmark) reactive transport simulation* based on full GEM calculations performed in every cell of each time step . The plots *on the right* are the chemical fields produced during the same simulation but *applying the ODML algorithm* with $\varepsilon = 0.01$.



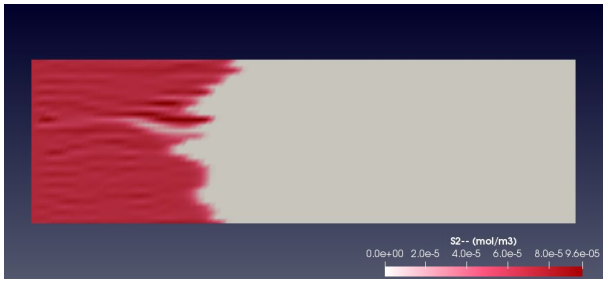
(a) step 100 (b) step 200

(c) step 400 (d) step 800

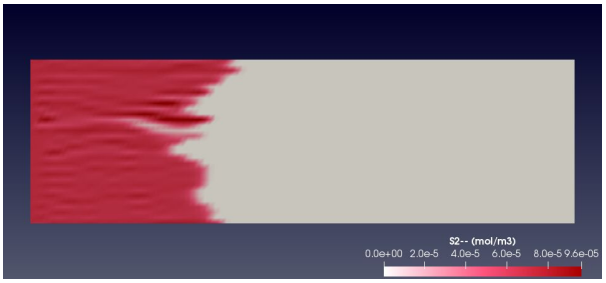
Figure 11: The amount of iron cation Fe^{2+} in the two-dimensional rock core at 100, 200, 400, and 800 time steps, corresponding to 35.26, 70.52, 141.04, and 282.08 days of simulations, respectively. The chemical fields are generated during the reactive transport simulation *using the ODML algorithm* for chemical equilibrium calculations with $\varepsilon = 0.01$.

front between siderite and pyrrhotite. Figure 12 confirms that the use of *the smart chemical equilibrium algorithm does not compromise accuracy during the simulation*, as the chemical fields on the left and the right are rather similar. The confirmation of this can be found in Figure 20 (see Appendix C), presenting the relative error obtained during the simulation run with the ODML method. The satisfaction of element mass balance conservation is also automatically in-build into the reconstructed species abundances . Figure 20(also in Appendix C) highlights that by showing the relative mass balance error of the selected elements.

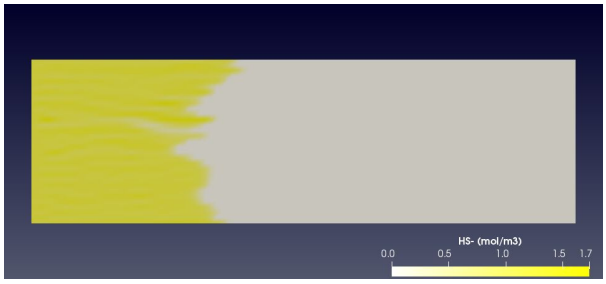
Number of on-demand learning operations. Next, we study the dependence of *the number of on-demand learnings* (full chemical equilibrium calculations using a conventional Newton-based algorithm) on the ODML's error control tolerance. In Figure 13, the number of required full evaluations can reach up to 60, 22, or 20, depending on the selected tolerances $\varepsilon = 0.001$, $\varepsilon = 0.005$, or $\varepsilon = 0.01$, respectively. As the injected brine moves down the rock core, way less additional learnings are performed to fulfill a given accuracy criterion. In fact, we see that triggered learnings are only required up until 1,300 steps. To highlight the overall number of on-demand trainings needed for each tolerance selected for the ODML run, we include them in the legend of Figure 13. This number is followed by the percentage it accounts from the total 6,262,000 chemical equilibrium problems that must be evaluated along the whole simulation process. As expected, the highest total number of learnings (almost 10 times higher than the others) correspond to the strictest tolerance $\varepsilon = 0.001$ (red marker). Similar to the previous examples, due to heterogeneity of the medium, the velocity changes might cause bigger perturbations during the later transport step and, as a result, different initial chemical compositions for the ODML algorithm. It explains the occasional increase in learnings per time step, see, e.g., time steps 900-1,100 in Fig-



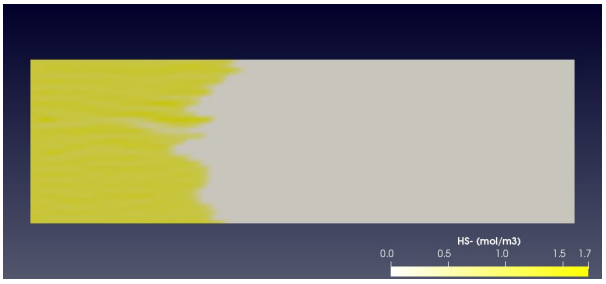
(a) S_2^{2-} with the conventional algorithm



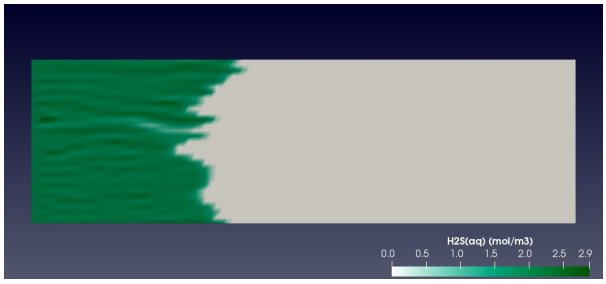
(b) S_2^{2-} with the ODML algorithm



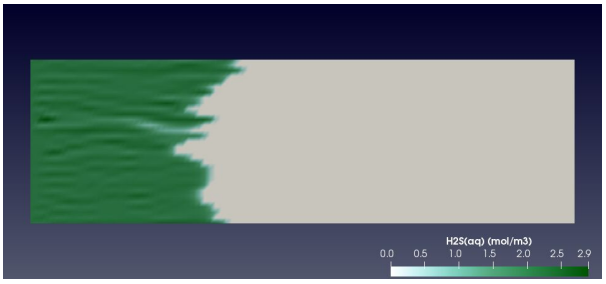
(c) HS^- with the conventional algorithm



(d) HS^- with the ODML algorithm



(e) H_2S (aq) with the conventional algorithm

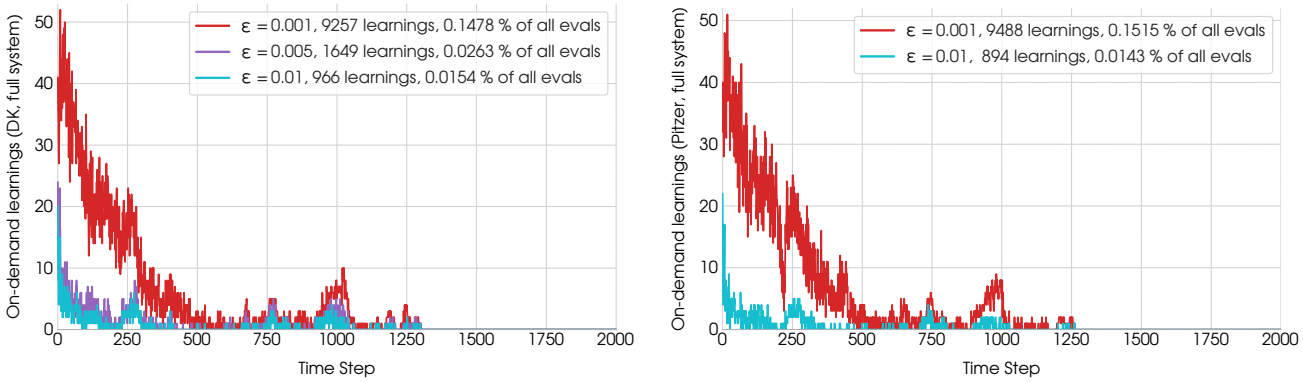


(f) H_2S (aq) with the ODML algorithm

Figure 12: The amount of sulfides S_2^{2-}, HS^-, and H_2S (aq) in the two-dimensional rock core at the time step 400. The chemical fields *on the left* are generated during the benchmark reactive transport simulation based *on full GEM calculations* performed in every cell of each time step. The plots *on the right* are the results of the similar numerical test *using the ODML algorithm* with $\varepsilon = 0.01$.

ure 13. Nevertheless, independent of the tolerance, **about 99.98% of all chemical states are approximated using smart predictions** based on the priority-based clustering combined with the first-order Taylor extrapolation. For the Pitzer activity model, the total number of learnings is slightly smaller for more relaxed tolerance $\varepsilon = 0.01$ and higher for $\varepsilon = 0.001$, even though the profile of occurring training per time step looks rather similar in Figure 13a and Figure 13b.

Computing cost reduction using ODML (when the Debye-Hückel activity model is used). Figure 14a compares the computational cost (measured in seconds) at each time step of *(i)* conventional chemical equilibrium calculations, *(ii)* smart chemical equilibrium calculations (run with $\varepsilon = 0.001$, $\varepsilon = 0.005$, or $\varepsilon = 0.01$), and *(iii)* transport calculations. The CPU time for the equilibrium calculations, both conventional and smart, is determined as a sum of all equilibrium states throughout all 3,131 mesh cells within the same time step. The transport cost comprises the time needed to solve the algebraic transport equations generated by the SUPG method. Even though



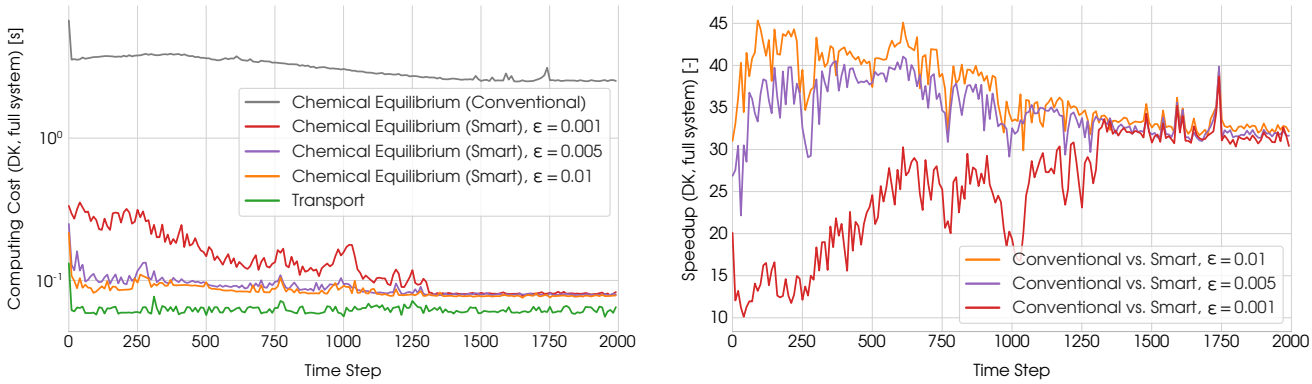
(a) the Debye-Hückel activity model

(b) the Pitzer activity model

Figure 13: The number of *on-demand learning operations* triggered by the ODML algorithm at each reactive transport time step for different ε using (a) the Debye-Hückel activity model and (b) the Pitzer activity model. Each learning requires the full solution of the non-linear equations governing chemical equilibrium using the Newton-based numerical method. We run simulations for 2,000 time steps, where each of such steps requires the solution of 6,262,000 chemical equilibrium problems. Legend depicts the accumulated/total number of *on-demand learning operations* triggered by the ODML algorithm for each of the considered tolerances and the percentage this number accounts from the total number of chemical states evaluations.

we consider the heterogeneous two-dimensional problem, transport costs remain over 1.5 times slower than the CPU costs of conventional chemical equilibrium calculations. **The ODML algorithm manages to decrease CPU costs of the chemical simulation by about one order of magnitude**. We see that reactive transport simulations using the smart approach with $\varepsilon = 0.001$ have the highest costs (red marker) with occasional spikes, e.g., between time steps 900 and 1100, corresponding to higher learnings rates. Next to the computation costs, we present speedup that the ODML can achieve in chemical calculations compared to the conventional approach. We see that the average speedup with the Debye-Hückel activity model is over 30x times except for $\varepsilon = 0.001$ on the first 1,200-1,300 steps. Nevertheless, the speedup is stabilized eventually around the value 33x, independent of how much overall trainings were performed and stored on the first steps. It confirms the efficiency of the reference chemical state retrieval when the priority-based cluster is incorporated.

Computing cost reduction using ODML (when the Pitzer activity model is used). For comparison, we also run a similar calculation using the Pitzer activity model (see Figure 15). These plots show the difference in computation costs when reactive transport is performed using either the Debye-Hückel or the Pitzer activity model. Figure 15a indicates that the CPU costs (per time step) using the conventional approach (grey curve) is of two orders of magnitude higher than in Figure 14a. We also see that the grey curve is at least three orders of magnitude higher than transport costs (green curve). The blue and red curves, corresponding to the reactive transport simulation with the ODML method, indicate that the smart approach drastically improves the cost of the conventional calculations, bringing it close to the cost of transport. The corresponding speedup presented in Figure 15b has initially relatively low values due to the high amount of trainings, then reaches 3500x (for blue line) and 2500x (for red line) on some time steps, and finally stabilizes around 2000x value. In contrast to the first example, we achieve a much higher



(a) CPU computing costs

(b) speedups

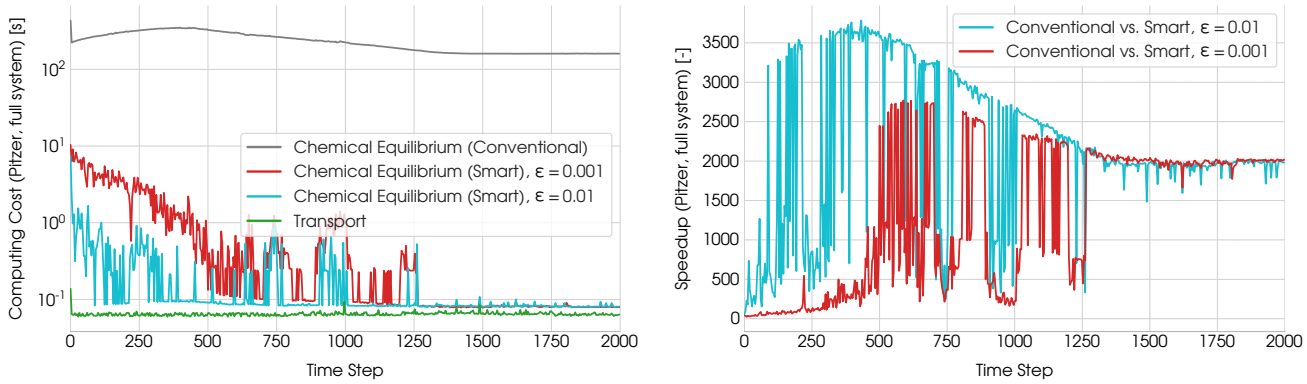
Figure 14: (a) Comparison of the computing costs (CPU time in seconds) of transport, conventional, and smart chemical equilibrium calculations during each time step of the reactive transport simulation for different ε. The cost of equilibrium calculations per time step is calculated as the sum of the individual costs in each degree of freedom, whereas the cost of transport calculations per time step is the time required when solving the discretized algebraic transport equations. (b) The speedup factor of chemical equilibrium calculations, at each time step of the simulation, resulting from the use of the ODML acceleration strategy with different ε. These calculations are performed using the *Debye-Hückel activity model* for the aqueous species.

acceleration in the numerical scavenging test (especially using the Pitzer activity model). To understand the accuracy of the reconstructed chemical fields generated by the ODML algorithm with $\varepsilon = 0.01$ and $\varepsilon = 0.001$, we compare them in Figure 15. We see that the transformation front between siderite dissolution and pyrrhotite precipitation is reconstructed rather exact, even though Figure 16a has a more uneven distribution of siderite (indicated by the different shades of blue). The **summary of the ODML performance for different tolerances and activity models** is presented in Figure 17b.

Clustering during the simulation process. Similar to the previous section, we present the clusters created during the run of the reactive transport simulation with the ODML algorithm, where tolerance is fixed to $\varepsilon = 0.01$. Table 6 lists only those that were successfully used for the reference chemical states more than twice (to shirk the number of presented clusters). We keep the numbering they were created during the test according to their original order (which explains skipped cluster numbers 9, 15, for instance). The primary species of presented clusters have some species that keep constant positions, such as H_2O(l), Cl^-, Na^+, Mg^{2+}, SO_4^{2-}, K^+, Ca^{2+} , whereas some other species, such as minerals siderite, pyrrhotite, carbonate-containing species HCO_3^-, CO_2(aq), $MgCO_3$(aq), sulfides H_2S (aq), HS^-, and iron-containing species FeO^+, FeO^+, Fe^{2+}, $HFeO_2$(aq) are constantly changing their place. Siderite is stable in Clusters 2–10, 12, 16, 19-20, 23, 25, 28, 31, 34, but unstable in those that reflect chemical states with completely dissolved mineral. Clusters 1, 10–11, 14, 17-18, 21-22, 29-30 correspond to chemical states where pyrrhotite is precipitated. Finally, equilibrium states, where neither of the minerals is present, are reflected by Clusters 13, 24, 26-27, and 36-46. Cluster 21 is the most often used for suitable reference equilibrium states that helped with accurate approximations of the ODML algorithm. Only two states stored in this cluster were used **3,899,826 times in the Taylor extrapolation**, which carries responsibility for **62.27% of all smart predictions**.

Table 6: Clusters created by the ODML algorithm (with $\varepsilon = 0.01$) during the reactive transport simulation of the chemical system with 79 aqueous species using the Debye-Hückel activity model. We present 38 clusters (selected out of the total 46) which were used more than twice by the ODML for the quick and smart predictions. *Clusters #* reflects the order they were created during the reactive transport simulation. *Frequency / Rank* is the number of times the cluster was used to retrieve the suitable reference equilibrium state for equilibrium state prediction. Column *Records* lists the number of fully calculated and stored chemical equilibrium states in the cluster.

Clusters #	**Primal Species**	**Frequency / Rank**	**# of Records**
1	$H_2O(l)$ Cl^- Na^+ Mg^{2+} SO_4^{2-} K^+ Ca^{2+} Pyrrhotite HCO_3^- $CO_2(aq)$ Siderite	119,835	1
2	$H_2O(l)$ Cl^- Na^+ Mg^{2+} SO_4^{2-} K^+ Ca^{2+} Siderite HCO_3^- $HFeO_2(aq)$ $MgCO_3(aq)$	4,444	3
3	$H_2O(l)$ Cl^- Na^+ Mg^{2+} SO_4^{2-} K^+ Ca^{2+} Siderite HCO_3^- Pyrrhotite $MgCO_3(aq)$	116	1
4	$H_2O(l)$ Cl^- Na^+ Mg^{2+} SO_4^{2-} K^+ Ca^{2+} Siderite HCO_3^- $MgCO_3(aq)$ $HFeO_2(aq)$	712,472	24
5	$H_2O(l)$ Cl^- Na^+ Mg^{2+} SO_4^{2-} K^+ Ca^{2+} Siderite HCO_3^- $MgCO_3(aq)$ Pyrrhotite	256	1
6	$H_2O(l)$ Cl^- Na^+ Mg^{2+} SO_4^{2-} K^+ Ca^{2+} Siderite HCO_3^- $MgCO_3(aq)$ HS^-	12,147	108
7	$H_2O(l)$ Cl^- Na^+ Mg^{2+} SO_4^{2-} K^+ Ca^{2+} Siderite HCO_3^- $HFeO_2(aq)$ FeO^+	5,492	3
8	$H_2O(l)$ Cl^- Na^+ Mg^{2+} SO_4^{2-} K^+ Ca^{2+} HCO_3^- Siderite $HFeO_2(aq)$ FeO^+	1,954	1
10	$H_2O(l)$ Cl^- Na^+ Mg^{2+} SO_4^{2-} K^+ Ca^{2+} Siderite HCO_3^- Pyrrhotite $CO_2(aq)$	310	1
11	$H_2O(l)$ Cl^- Na^+ Mg^{2+} SO_4^{2-} K^+ Ca^{2+} Pyrrhotite HCO_3^- $CO_2(aq)$ $H_2S(aq)$	43,065	8
12	$H_2O(l)$ Cl^- Na^+ Mg^{2+} SO_4^{2-} K^+ Ca^{2+} Siderite HCO_3^- $CO_2(aq)$ $HFeO_2(aq)$	63,669	19
13	$H_2O(l)$ Cl^- Na^+ Mg^{2+} SO_4^{2-} K^+ Ca^{2+} HCO_3^- $FeO^+HFeO_2(aq)$ $O_2(aq)$	40	49
14	$H_2O(l)$ Cl^- Na^+ Mg^{2+} SO_4^{2-} K^+ Ca^{2+} Pyrrhotite $H_2S(aq)$ HS^- HCO_3^-	383,052	25
16	$H_2O(l)$ Cl^- Na^+ Mg^{2+} SO_4^{2-} K^+ $Ca^{2+}HCO_3^-$ $FeO^+HFeO_2(aq)$ Siderite	1,466	1
17	$H_2O(l)$ Cl^- Na^+ Mg^{2+} SO_4^{2-} K^+ Ca^{2+} Pyrrhotite $CO_2(aq)$ HCO_3^- $H_2S(aq)$	4,176	6
18	$H_2O(l)$ Cl^- Na^+ Mg^{2+} SO_4^{2-} K^+ Ca^{2+} Pyrrhotite $HCO_3^-CO_2(aq)$ Fe^{2+}	3,759	4
19	$H_2O(l)$ Cl^- Na^+ Mg^{2+} SO_4^{2-} K^+ Ca^{2+} Siderite $HCO_3^-CO_2(aq)$ FeO^+	825,867	31
20	$H_2O(l)$ Cl^- Na^+ Mg^{2+} SO_4^{2-} K^+ Ca^{2+} Siderite $HCO_3^-CO_2(aq)$ HS^-	25,644	81
21	$H_2O(l)$ Cl^- Na^+ Mg^{2+} SO_4^{2-} K^+ Ca^{2+} Pyrrhotite $H_2S(aq)$ $HCO_3^-CO_2(aq)$ Fe^{2+}	3,899,826	2
22	$H_2O(l)$ Cl^- Na^+ Mg^{2+} SO_4^{2-} K^+ Ca^{2+} Pyrrhotite $H_2S(aq)$ HCO_3^- HS^-	1207	4
23	$H_2O(l)$ Cl^- Na^+ Mg^{2+} SO_4^{2-} K^+ Ca^{2+} Siderite $HCO_3^-CO_2(aq)$ $H_2S(aq)$	67,448	26
24	$H_2O(l)$ Cl^- Na^+ Mg^{2+} SO_4^{2-} K^+ Ca^{2+} HCO_3^- $FeO^+CO_2(aq)$ $O_2(aq)$	73	91
25	$H_2O(l)$ Cl^- Na^+ Mg^{2+} SO_4^{2-} K^+ Ca^{2+} HCO_3^-Siderite $CO_2(aq)$ FeO^+	80,302	2
26	$H_2O(l)$ Cl^- Na^+ Mg^{2+} SO_4^{2-} K^+ Ca^{2+} HCO_3^- $CO_2(aq)$ FeO^+ $O_2(aq)$	744	294
27	$H_2O(l)$ Cl^- Na^+ Mg^{2+} SO_4^{2-} K^+ Ca^{2+} HCO_3^- $CO_2(aq)$ FeO^+ Fe^{2+}	260	16
28	$H_2O(l)$ Cl^- Na^+ Mg^{2+} SO_4^{2-} K^+ Ca^{2+} Siderite $HCO_3^-HFeO_2(aq)$ $CO_2(aq)$	9	1
29	$H_2O(l)$ Cl^- Na^+ Mg^{2+} SO_4^{2-} K^+ Ca^{2+} HCO_3^- $CO_2(aq)$ Pyrrhotite $H_2S(aq)$	9	2
30	$H_2O(l)$ Cl^- Na^+ Mg^{2+} SO_4^{2-} K^+ Ca^{2+} HCO_3^- Pyrrhotite $CO_2(aq)$ $H_2S(aq)$	9	3
31	$H_2O(l)$ Cl^- Na^+ Mg^{2+} SO_4^{2-} K^+ Ca^{2+} HCO_3^- FeO^+Siderite $HFeO_2(aq)$	296	1
34	$H_2O(l)$ Cl^- Na^+ Mg^{2+} SO_4^{2-} K^+ Ca^{2+} HCO_3^- $FeO^+CO_2(aq)$ Siderite	2,622	1
36	$H_2O(l)$ Cl^- Na^+ Mg^{2+} SO_4^{2-} K^+ Ca^{2+} HCO_3^- $CO_2(aq)$ $O_2(aq)$ FeO^+	15	59
39	$H_2O(l)$ Cl^- Na^+ Mg^{2+} SO_4^{2-} K^+ Ca^{2+} $CO_2(aq)$ HCO_3^- $FeO^+O_2(aq)$	5	13
41	$H_2O(l)$ Cl^- Na^+ Mg^{2+} SO_4^{2-} K^+ Ca^{2+} $CO_2(aq)$ HCO_3^- FeO^+Fe^{2+}	3	4
42	$H_2O(l)$ Cl^- Na^+ Mg^{2+} SO_4^{2-} K^+ Ca^{2+} $CO_2(aq)$ HCO_3^- $H_2S(aq)$ Fe^{2+}	53	8
43	$H_2O(l)$ Cl^- Na^+ Mg^{2+} SO_4^{2-} K^+ Ca^{2+} $CO_2(aq)$ HCO_3^- $H_2S(aq)$ $FeCl^+$	18	4
44	$H_2O(l)$ Cl^- Na^+ Mg^{2+} SO_4^{2-} K^+ Ca^{2+} $CO_2(aq)$ HCO_3^- $H_2S(aq)$ FeO^+	68	2
46	$H_2O(l)$ Cl^- Na^+ Mg^{2+} SO_4^{2-} K^+ Ca^{2+} $H_2S(aq)$ HS^- $HCO_3^-Fe^{2+}$	318	1



(a) CPU computing costs

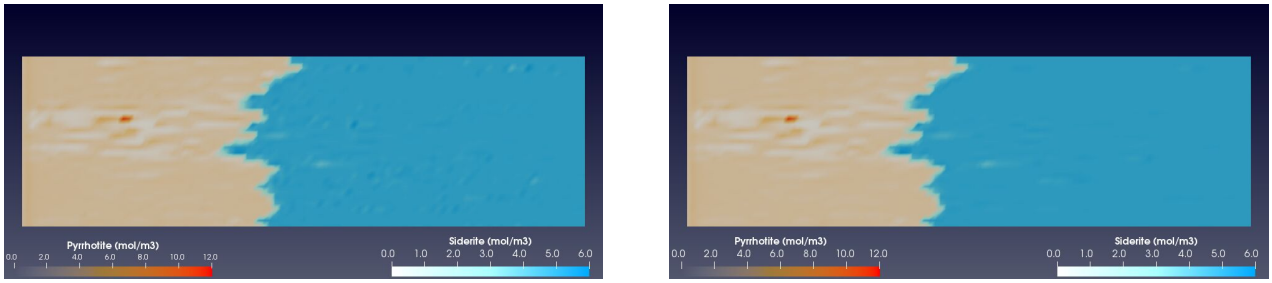
(b) speedups

Figure 15: (a) Comparison of the computing costs (CPU time in seconds) of transport, conventional, and smart chemical equilibrium calculations during each time step of the reactive transport simulation for different ε. The cost of equilibrium calculations per time step is determined as the sum of the individual costs in each degree of freedom, whereas the cost of transport calculations per time step is the time required when solving the discretized algebraic transport equations. (b) The speedup factor of chemical equilibrium calculations, at each time step of the simulation, resulting from the use of the on-demand learning acceleration strategy with different ε. All the calculations are performed using the *Pitzer activity model* for the aqueous species.

5 Discussion and Conclusions

The coupling of Reaktoro and Firedrake enabled us to study the performance of the new ODML algorithm on more challenging reactive transport problems. The obtained numerical results confirm that the resulting acceleration of the chemical equilibrium calculations provided by the new acceleration strategy depends on several factors. The first and most important one is the activity models used for the aqueous species in the numerical experiment. The second is the chosen error control/accuracy tolerances (parameter ϵ), which determines how strict the acceptance criterion is. Finally, the obtained acceleration depends on the complexity of the numerical reactive transport experiment, e.g., chemical system size, heterogeneity, mesh dimension, etc. Having said that, the ODML algorithm enables speedups of **one to three orders of magnitude in chemical equilibrium calculation** and **at least one order of magnitude of overall reactive transport simulations**. We remark that an important important property of ODML strategy is its ability to converse mass of chemical elements (and also electric charge) to machine precision levels. This inherent feature of the algorithm is explained and demonstrated mathematically in Leal et al. (2020), and it is a capability not naturally found in conventional machine learning algorithms (e.g., neural network and most classes of surrogate models).

To highlight the **key performance characteristics of the ODML algorithm**, we use Figures 17a and 17b. In particular, we recap the overall number of learnings each simulation run required for different tolerances and activity models. Besides, we emphasize that **the percentage of smart predictions remains greater than 99.8%** with respect to the total number of chemical equilibrium problems in the entire simulation. We also include the **lowest and highest speedups in chemical equilibrium calculations** throughout all the time steps and the **overall speedups in the reactive transport simulations** achieved by using the ODML method.



(a) $\varepsilon = 0.01$ (b) $\varepsilon = 0.001$

Figure 16: Comparison of the amount of minerals siderite and pyrrhotite (in mol/m^3) in the two-dimensional rock core at time step 500 generated by the reactive transport simulation using the ODML algorithm with different tolerances (a) $\varepsilon = 0.01$ and (b) $\varepsilon = 0.001$.

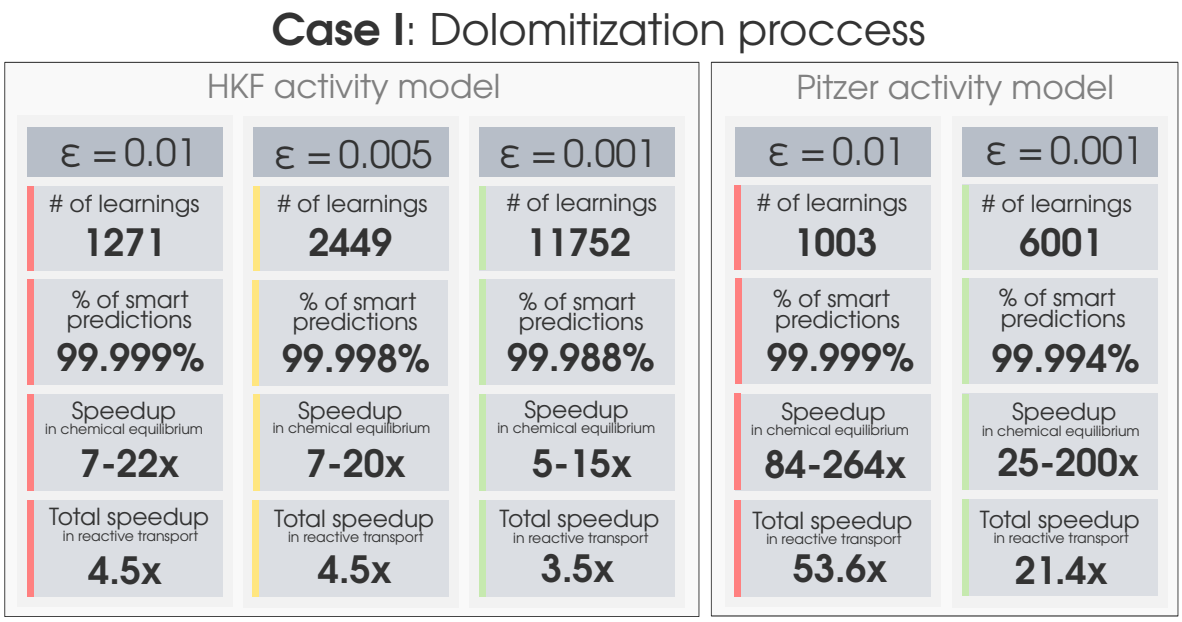
In future works, we aim to apply the on-demand machine learning (ODML) strategy to accelerate modeling of chemical kinetics with partial chemical equilibrium assumptions, typical in geochemical systems. We also consider further investigations with more complex geochemical and geological conditions. We plan to extend Reaktoro's functionality to model reservoirs souring as a result of the activities of sulfide-reducing bacteria, mixing of the groundwater and seawater in the oil reservoir as well as scaling effects this process results to, modeling the effects that seawater or sodium chloride have during the cement rock attack, among many more. An extension to the three-dimensional problem with heterogeneity will require the further implementation of a stable numerical scheme to solve the Darcy problem. To enable full coupling of the transport and flow problems, we plan to continue developing the reactive transport simulator and present obtained results in the future articles.

Acknowledgments

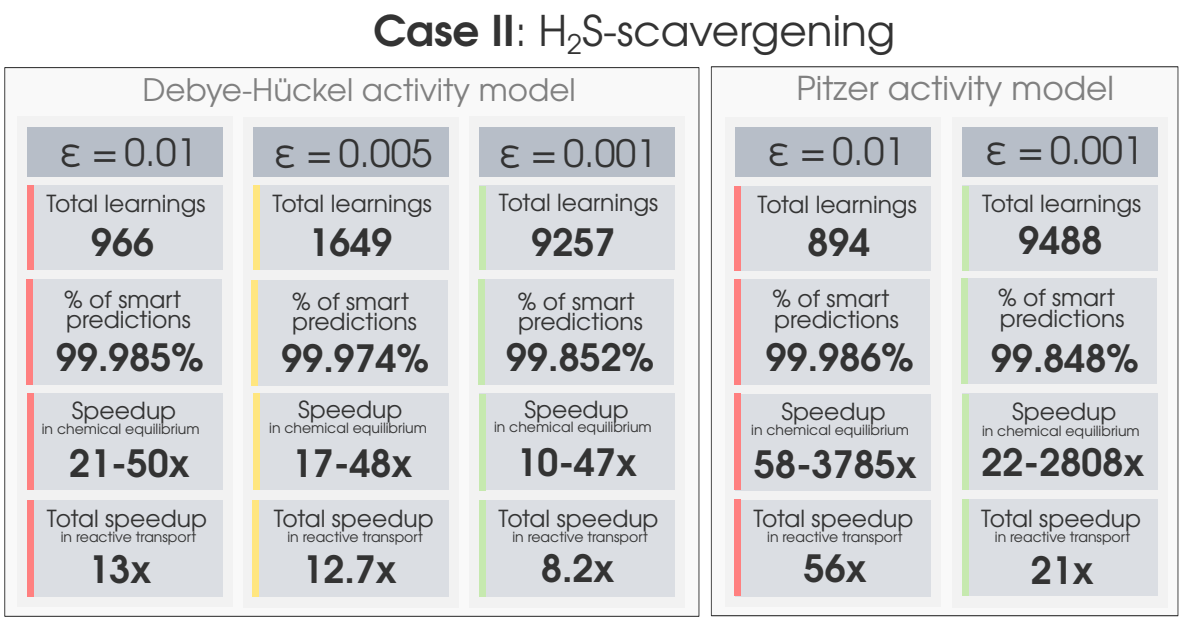
This research project is funded by the Swiss National Science Foundation (Ambizione Grant PZ00P2-179967), the Werner Siemens Foundation, and Shell Global Solutions International BV. We thank these organizations for their financial support.

CRediT authorship contribution statement

- **Svetlana Kyas**: Conceptualization, Formal analysis, Methodology, Software, Investigation, Validation, Writing - original draft, Writing - review & editing.
- **Diego Volpatto**: Conceptualization, Formal analysis, Methodology, Software, Investigation, Validation, Writing - review & editing.
- **Martin O. Saar**: Funding acquisition, Writing - review & editing.
- **Allan M. M. Leal**: Funding acquisition, Conceptualization, Formal analysis, Methodology, Software, Investigation, Validation, Writing - review & editing.



(a)



(b)

Figure 17: Summary of the total number of learning operations,the percentage of the smart predictions with respect to the total number of the chemical equilibrium calculations, the range of speedups in chemical equilibrium calculations throughout all time steps, and the total reactive transport simulation speedups for different tolerances (a) using the HKF and the Pitzer activity models in the dolomitization example and (b) using the Debye-Hückel and the Pitzer activity models in the scavenging example.

References

Leal, A. M. M., Kyas, S., Kulik, D. A., and Saar, M. O. (2020). Accelerating reactive transport modeling: on-demand machine learning algorithm for chemical equilibrium calculations. *Transp. Porous Media*, 133(2):161–204.

Rathgeber, F., Ham, D. A., Mitchell, L., Lange, M., Luporini, F., McRae, A. T., Bercea, G. T., Markall, G. R., and Kelly, P. H. (2016). Firedrake: Automating the finite element method by composing abstractions. *ACM Transactions on Mathematical Software*, 43(3).

Leal, A. M. (2015). Reaktoro: A unified framework for modeling chemically reactive systems.

Steefel, C., Depaolo, D., and Lichtner, P. (2005). Reactive transport modeling: An essential tool and a new research approach for the Earth sciences. *Earth and Planetary Science Letters*, 240(3-4):539–558.

Xiao, Y., Whitaker, F., Xu, T., and Steefel, C. (2018). *Reactive transport modeling: Applications in subsurface energy and environmental problems*.

Steefel, C. I. (2019). Reactive Transport at the Crossroads. *Reviews in Mineralogy and Geochemistry*, 85(1):1–26.

Smith, W. and Missen, R. (1982). *Chemical reaction equilibrium analysis: theory and algorithms*. Wiley-Interscience, New York.

Zeleznik, F. J. and Gordon, S. (1960). An analytical investigation of the general methods of calculating chemical equilibrium compositions. Technical Report NASA-TN-D-473, NASA.

Leal, A. M., Kulik, D. A., and Saar, M. O. (2016). Enabling Gibbs energy minimization algorithms to use equilibrium constants of reactions in multiphase equilibrium calculations. *Chemical Geology*, 437:170–181.

Parkhurst, D. and Appelo, C. (1999). User's guide to PHREEQC (Version 2)—A computer program for speciation, batch-reaction, one-dimensional transport, and inverse geochemical calculations. *USGS Water-Resources Investigations Report*, 99(4259):326.

Samper, J., Juncosa, R., Delgado, J., and Montenegro, L. (2000). CORE . A code for non-isothermal water flow and reactive solute transport. Users manual version 2. (January).

Jang, E., Boog, J., He, W., and Kalbacher, T. (2018). *Computational Hydrology III: OGS-PHREEQC coupled reactive transport modeling*. Springer International Publishing.

Lichtner, P. C., Hammond, G. E., Lu, C., Karra, S., Bisht, G., Andre, B., Mills, R. T., Kumar, J., and Frederick, J. M. (2019). Opengeosys. OpenGeoSys (OGS) is a scientific open source project for the development of numerical methods for the simulation of thermo-hydro-mechanical-chemical (THMC) processes in porous and fractured media.

Simunek, J. and van Genuchten, M. (2014). Kinetics of lime/bentonite pozzolanic reactions at 20 and 50 °C: Batch tests and modeling. *Cem. Concr. Res.*, 59(2):34–42.

Meeussen, J. (2003). ORCHESTRA: An object-oriented frame- work for implementing chemical equilibrium models. Technical Report 37.

Bächler, D. and Kohl, T. (2005). Coupled thermal-hydraulic-chemical modelling of enhanced geothermal systems. *Geophysical Journal International*, 161(2):533–548.

Xu, T., Sonnenthal, E., Spycher, N., and Pruess, K. (2006). TOUGHREACT - A simulation program for non-isothermal multiphase reactive geochemical transport in variably saturated geologic media: Applications to geothermal injectivity and CO2 geological sequestration. *Computers & Geosciences*, 32(2):145–165.

White, M. and Oostrom, M. (2006). Stomp subsurface transport over multiple phases version 4.0 user's guide. Technical report.

Bethke, C. M. (2007). *Geochemical and Biogeochemical Reaction Modeling*. Cambridge University Press, New York, 2nd edition.

Kulik, D., Berner, U. R., and Curti, E. (2004). Modeling chemical equilibrium partitioning with the GEMS-PSI code. Technical Report March, Paul Scherrer Institut, Villigen, Switzerland.

Kulik, D. A., Wagner, T., Dmytrieva, S. V., Kosakowski, G., Hingerl, F. F., Chudnenko, K. V., and Berner, U. R. (2013). GEM-Selektor geochemical modeling package: revised algorithm and GEMS3K numerical kernel for coupled simulation codes. *Computational Geosciences*, 17(1):1–24.

Yeh, G., Tsai, C., and Ni, C. (2013). Hydrogeochem 6.0: A model to couple thermal-hydrology-mechanics-chemical (thmc) processes user guide. Technical report.

Gamazo, P., Slooten, L. J., Carrera, J., Saaltink, M. W., Bea, S., and Soler, J. (2016). PROOST: Object-oriented approach to multiphase reactive transport modeling in porous media. *Journal of Hydroinformatics*, 18(2):310–328.

Steefel, C. I. (2009). Crunchflow: Software for modeling multicomponent reactive flow and transport. Technical report.

Mayer, K. e. (2020). Min3p: The reactive transport code min3p: Multicomponent reactive transport modeling in variably saturated porous media.

Lichtner, P. C., Hammond, G. E., Lu, C., Karra, S., Bisht, G., Andre, B., Mills, R. T., Kumar, J., and Frederick, J. M. (2019). PFLOTRAN Web page. http://www.pflotran.org.

Langevin, C., Hughes, J., Banta, E., Provost, A., Niswonger, R., and Panday, S. (2019). MODFLOW 6 Modular Hydrologic Model version 6.1.0: U.S. Geological Survey Software Release.

Steefel, C. I., Appelo, C. A. J., Arora, B., Jacques, D., Kalbacher, T., Kolditz, O., Lagneau, V., Lichtner, P. C., Mayer, K. U., Meeussen, J. C. L., Molins, S., Moulton, D., Shao, H., Šimůnek, J., Spycher, N., Yabusaki, S. B., and Yeh, G. T. (2015). Reactive transport codes for subsurface environmental simulation. *Computational Geosciences*, 19(3):445–478.

Jacques, D. and Simunek, J. (2005). User manual of the multicompenent variably-saturated ow and transport model hp1.

Simunek, J. and van Genuchten, M. (2008). Modeling non-equilibrium flow and transport processes using HYDRUS. *Vadose Zone J.*, 7(2):782–797.

Parkhurst, D. and Appelo, C. (2013). Description of input and examples for PHREEQC version 3—A computer program for speciation, batch-reaction, one-dimensional transport, and inverse geochemical calculations. In *Groundwater Book 6, Modeling Techniques*, chapter A43, page 497. U.S. Geological Survey Techniques and Methods.

Zheng, C. and Wang, P. (1999). Mt3dms: A modular three-dimensional multispecies transport model for simulation of advection, dispersion and chemical reactions of contaminants in ground water systems: documentation and user's guide. Technical report. http://hydro.geo.ua.edu/mt3d.

Nardi, A., Idiart, A., Trinchero, P., De Vries, L. M., and Molinero, J. (2014). Interface COMSOL-PHREEQC (iCP), an efficient numerical framework for the solution of coupled multiphysics and geochemistry. *Computers and Geosciences*, 69:10–21.

Guo, B., Hong, Y., Qiao, G., and Ou, J. (2018). A COMSOL-PHREEQC interface for modeling the multi-species transport of saturated cement-based materials. *Construction and Building Materials*, 187:839–853.

Azad, V. J., Li, C., Verba, C., Ideker, J. H., and Isgor, O. B. (2016). A COMSOL-GEMS interface for modeling coupled reactive-transport geochemical processes. *Computers and Geosciences*, 92:79–89.

Yapparova, A., Gabellone, T., Whitaker, F., Kulik, D. A., and Matthäi, S. K. (2017). Reactive Transport Modelling of Dolomitisation Using the New CSMP++GEM Coupled Code: Governing Equations, Solution Method and Benchmarking Results. *Transport in Porous Media*, 117(3):385–413.

Elakneswaran, Y. and Ishida, T. (2014). Development and verification of an integrated physicochemical and geochemical modelling framework for performance assessment of cement-based materials. *Journal of Advanced Concrete Technology*, 12(4):111–126.

Centler, F., Shao, H., De Biase, C., Park, C. H., Regnier, P., Kolditz, O., and Thullner, M. (2010). GeoSysBRNS-A flexible multidimensional reactive transport model for simulating biogeochemical subsurface processes. *Computers and Geosciences*, 36(3):397–405.

Muniruzzaman, M. and Rolle, M. (2016). Modeling multicomponent ionic transport in groundwater with IPhreeqc coupling: Electrostatic interactions and geochemical reactions in homogeneous and heterogeneous domains. *Advances in Water Resources*, 98:1–15.

Li, D., Bauer, S., Benisch, K., Graupner, B., and Beyer, C. (2014). OpenGeoSys-ChemApp: A coupled simulator for reactive transport in multiphase systems and application to CO2 storage formation in Northern Germany. *Acta Geotechnica*, 9(1):67–79.

Kosakowski, G. and Watanabe, N. (2014). OpenGeoSys-Gem: A numerical tool for calculating geochemical and porosity changes in saturated and partially saturated media. *Physics and Chemistry of the Earth*, 70-71:138–149.

He, W., Beyer, C., Fleckenstein, J. H., Jang, E., Kolditz, O., Naumov, D., and Kalbacher, T. (2015). A parallelization scheme to simulate reactive transport in the subsurface environment with OGS#IPhreeqc 5.5.7-3.1.2. *Geoscientific Model Development*, 8(10):3333–3348.

Georget, F., Prévost, J. H., and Huet, B. (2017). A reactive transport simulator for variable porosity problems. *Computational Geosciences*, 21(1):95–116.

Jara, D., de Dreuzy, J. R., and Cochepin, B. (2017). TReacLab: An object-oriented implementation of non-intrusive splitting methods to couple independent transport and geochemical software. *Computers and Geosciences*, 109(September):281–294.

Damiani, L. H., Kosakowski, G., Glaus, M. A., and Churakov, S. V. (2020). A framework for reactive transport modeling using FEniCS–Reaktoro: governing equations and benchmarking results. *Computational Geosciences*, 24(3):1071–1085.

Leal, A. M., Blunt, M. J., and LaForce, T. C. (2014). Efficient chemical equilibrium calculations for geochemical speciation and reactive transport modelling. *Geochimica et Cosmochimica Acta*, 131:301–322.

Leal, A. M., Kulik, D. A., and Kosakowski, G. (2016). Computational methods for reactive transport modeling: A Gibbs energy minimization approach for multiphase equilibrium calculations. *Advances in Water Resources*, 88:231–240.

Leal, A. M. M., Kulik, D. A., Smith, W. R., and Saar, M. O. (2017). An overview of computational methods for chemical equilibrium and kinetic calculations for geochemical and reactive transport modeling. *Pure and Applied Chemistry*, 89(5):597–643.

Leal, A. M., Kulik, D. A., Kosakowski, G., and Saar, M. O. (2016). Computational methods for reactive transport modeling: An extended law of mass-action, xLMA, method for multiphase equilibrium calculations. *Advances in Water Resources*, 96:405–422.

Leal, A. M., Blunt, M. J., and LaForce, T. C. (2015). A chemical kinetics algorithm for geochemical modelling. *Applied Geochemistry*, 55:46–61.

Alnæ s, M. S., Logg, A., Ø lgaard, K. B., Rognes, M. E., and Wells, G. N. (2014). Unified form language: a domain-specific language for weak formulations and partial differential equations. *ACM Trans. Math. Software*, 40(2):Art. 9, 37.

Logg, A. and Wells, G. N. (2010). DOLFIN. *ACM Transactions on Mathematical Software*, 37(2):1–28.

Logg, A. and Wells, G. N. (2012). *Automated Solution of Differential Equations by the Finite Element Method*, volume 84 of *Lecture Notes in Computational Science and Engineering*. Springer Berlin Heidelberg, Berlin, Heidelberg.

Jasakh, H. (2012). OpenFOAM: Open source CFD in research and industry. *International Journal of Naval Architecture and Ocean Engineering*, (February 2014).

Oliveira, T. D., Blunt, M. J., and Bijeljic, B. (2019). Modelling of multispecies reactive transport on pore-space images. *Advances in Water Resources*, 127(August 2018):192–208.

Lichtner, P. C. (1985). Continuum model for simultaneous chemical reactions and mass transport in hydrothermal systems. *Geochimica et Cosmochimica Acta*, 49(3):779–800.

Peaceman, D. W. (1977). *Fundamental of Numerical Reservoir Simulation*. Elsevier, Amsterdam.

Brooks, A. N. and Hughes, T. J. R. (1982). Streamline upwind/Petrov-Galerkin formulations for convection dominated flows with particular emphasis on the incompressible Navier-Stokes equations. *Comput. Methods Appl. Mech. Engrg.*, 32(1-3):199–259. FENOMECH "81, Part I (Stuttgart, 1981).

Malta, S. M. C. and Loula, A. F. D. (1998). Numerical analysis of finite element methods for miscible displacements in porous media. *Numer. Methods Partial Differential Equations*, 14(4):519–548.

Malta, S. M. C., Loula, A. F. D., and Garcia, E. L. M. (2000). Numerical analysis of a stabilized finite element method for tracer injection simulations. *Comput. Methods Appl. Mech. Engrg.*, 187(1-2):119–136.

Brezzi, F. and Fortin, M. (2001). A minimal stabilisation procedure for mixed finite element methods. *Numer. Math.*, 89(3):457–491.

Masud, A. and Hughes, T. J. R. (2002). A stabilized mixed finite element method for Darcy flow. *Comput. Methods Appl. Mech. Engrg.*, 191(39-40):4341–4370.

Correa, M. R. and Loula, A. F. D. (2008). Unconditionally stable mixed finite element methods for Darcy flow. *Comput. Methods Appl. Mech. Engrg.*, 197(17-18):1525–1540.

Cockburn, B. and Gopalakrishnan, J. (2004). A characterization of hybridized mixed methods for second order elliptic problems. *SIAM Journal on Numerical Analysis*, 42(1):283–301.

Cockburn, B., Gopalakrishnan, J., and Lazarov, R. (2009). Unified hybridization of discontinuous Galerkin, mixed, and continuous Galerkin methods for second order elliptic problems. *SIAM J. Numer. Anal.*, 47(2):1319–1365.

Núñez, Y., Faria, C., Loula, A., and Malta, S. (2012). A mixed-hybrid finite element method applied to tracer injection processes. *International Journal of Modeling and Simulation for the Petroleum Industry*, 6.

Leal, A. M. M. et al. (2018). autodiff, a modern, fast and expressive C++ library for automatic differentiation. `https://autodiff.github.io`.

Pitzer, K. S. (1973). Thermodynamics of electrolytes. I. Theoretical basis and general equations. *The Journal of Physical Chemistry*, 77(2):268–277.

Harvie, C. E., Møller, N., and Weare, J. H. (1984). The prediction of mineral solubilities in natural waters: The Na-K-Mg-Ca-H-Cl-SO4-OH-HCO3-CO3-CO2-H2O system to high ionic strengths at 25°C. *Geochimica et Cosmochimica Acta*, 48(4):723–751.

Drummond, S. (1981). *Boiling and mixing of hydrothermal fluids: chemical effects on mineral precipitation*. Ph.d., Pennsylvania State University.

Debye, P. and Hückel, E. (1923). The theory of electrolytes. 1. lowering of freezing point and related phenomena. *Physikalische Zeitschrift*, 24:85–206.

Helgeson, H. C. and Kirkham, D. H. (1974a). Theoretical prediction of the thermodynamic behavior of aqueous electrolytes at high pressures and temperatures: I. Summary of the thermodynamic/electrostatic properties of the solvent. *American Journal of Science*, 274(10):1089–1198.

Helgeson, H. C. and Kirkham, D. H. (1974b). Theoretical prediction of the thermodynamic behavior of aqueous electrolytes at high pressures and temperatures: II. Debye-Huckel parameters for activity coefficients and relative partial molal properties. *American Journal of Science*, 274(10):1199–1261.

Helgeson, H. C. and Kirkham, D. H. (1976). Theoretical prediction of the thermodynamic properties of aqueous electrolytes at high pressures and temperatures: III. Equation of state for aqueous species at infinite dilution. *American Journal of Science*, 276(2):97–240.

Helgeson, H. C., Kirkham, D. H., and Flowers, G. C. (1981). Theoretical prediction of the thermodynamic behavior of aqueous electrolytes at high pressures and temperatures: IV. Calculation of activity coefficients, osmotic coefficients, and apparent molal and standard and relative partial molal properties to 600 C. *American Journal of Science*, 281(10):1249–1516.

Helgeson, H. C., Delany, J. M., Nesbitt, H. W., and Bird, D. K. (1978). Summary and critique of the thermodynamic properties of rock-forming minerals. *American Journal of Science*, 278 A(1):229.

Tanger, J. C. and Helgeson, H. C. (1988). Calculation of the thermodynamic and transport properties of aqueous species at high pressures and temperatures; revised equations of state for the standard partial molal properties of ions and electrolytes. *American Journal of Science*, 288(1):19–98.

Shock, E. and Helgeson, H. C. (1988). Calculation of the thermodynamic and transport properties of aqueous species at high pressures and temperatures: Correlation algorithms for ionic species and equation of state predictions to 5 kb and 1000°C. *Geochimica et Cosmochimica Acta*, 52(8):2009–2036.

Shock, E. L., Oelkers, E. H., Johnson, J. W., Sverjensky, D. A., and Helgeson, H. C. (1992). Calculation of the thermodynamic properties of aqueous species at high pressures and temperatures. Effective electrostatic radii, dissociation constants and standard partial molal properties to 1000 °C and 5 kbar. *Journal of the Chemical Society, Faraday Transactions*, 88(6):803.

Wagner, W. and Pruss, A. (2002). The IAPWS Formulation 1995 for the Thermodynamic Properties of Ordinary Water Substance for General and Scientific Use. *Journal of Physical and Chemical Reference Data*, 31(2):387.

Johnson, J. W., Oelkers, E. H., and Helgeson, H. C. (1992). SUPCRT92: A software package for calculating the standard molal thermodynamic properties of minerals, gases, aqueous species, and reactions from 1 to 5000 bar and 0 to 1000 C. *Computers & Geosciences*, 18(7):899–947.

Müller, S. and Schüler, L. (2019). Geostat-framework/gstools: Reverberating red (version v1.1.0). `http://doi.org/10.5281/zenodo.3468230`.

Núñez, Y. R., Faria, C. O., Malta, S. M. C., and Loula, A. F. D. (2018). The influence of velocity field approximations in tracer injection processes. *TEMA Tend. Mat. Apl. Comput.*, 19(2):347–367.

Arnold, D. N. and Brezzi, F. (1985). Mixed and nonconforming finite element methods: implementation, postprocessing and error estimates. *RAIRO Modél. Math. Anal. Numér.*, 19(1):7–32.

Nguyen, N. C., Peraire, J., and Cockburn, B. (2011). Hybridizable discontinuous galerkin methods. In *Spectral and High Order Methods for Partial Differential Equations*, pages 63–84. Springer.

Correa, M. R. and Loula, A. F. D. (2007). Stabilized velocity post-processings for Darcy flow in heterogeneous porous media. *Comm. Numer. Methods Engrg.*, 23(6):461–489.

Arnold, D. N., Brezzi, F., Cockburn, B., and Marini, L. D. (2001/02). Unified analysis of discontinuous Galerkin methods for elliptic problems. *SIAM J. Numer. Anal.*, 39(5):1749–1779.

Loula, A. F. D., Correa, M. R., Guerreiro, J. N. C., and Toledo, E. M. (2008). On finite element methods for heterogeneous elliptic problems. *Internat. J. Solids Structures*, 45(25-26):6436–6450.

Bochev, P. B. and Gunzburger, M. D. (1998). Finite element methods of least-squares type. *SIAM Rev.*, 40(4):789–837.

Núñez, Y. R., Faria, C. O., Loula, A. F. D., and Malta, S. M. C. (2017). A hybrid finite element method applied to miscible displacements in heterogeneous porous media. *Rev. Int. Métod. Numér. Cálc. Diseño Ing.*, 33(1-2):45–51.

Appendix A

To present the SDHM formulation used in this work, we introduce the classical L^2 inner-products for an arbitrary regular domain $\Omega \subset \mathbb{R}^n$ $(n = 2,3)$ as:

$$(p,q)_\Omega := \int_\Omega pq\,dx \qquad \langle p,q\rangle_{\partial\Omega} := \int_{\partial\Omega} pq\,ds$$
$$(\boldsymbol{v},\boldsymbol{w})_\Omega := \int_\Omega \boldsymbol{v}\cdot\boldsymbol{w}\,dx \qquad \langle \boldsymbol{v},\boldsymbol{w}\rangle_{\partial\Omega} := \int_{\partial\Omega} \boldsymbol{v}\cdot\boldsymbol{w}\,ds$$

in which p and q are scalar functions and $\boldsymbol{v}$ and $\boldsymbol{w}$ vector-valued functions defined on Ω.

To derive the weak formulation of the Darcy problem (2) in the heterogeneous medium, we follow the lines of Núñez et al. (2018). Let $\mathcal{T}_h := \{\mathcal{K}\}$ be a regular tessellation of the domain Ω, such that $\Omega = \bigcup_{\mathcal{K}} \mathcal{K}$. Let $\mathcal{E}_h := \{e : e \subset \partial K,\ \mathcal{K} \in \mathcal{T}_h\}$ denote the set of edges, where e is the edge of the element $\mathcal{K}$. Let $\mathcal{E}_h^0 \subset \mathcal{E}_h$ denote a subset of interior edges. Thus, we obtain the following weak form of (2):

$$(\mu\kappa^{-1}\boldsymbol{u},\boldsymbol{w})_\mathcal{K} - (p,\nabla\cdot\boldsymbol{w})_\mathcal{K} + \int_{\partial\mathcal{K}} \hat{p}\,(\boldsymbol{w}\cdot\boldsymbol{n}_\mathcal{K})\,ds = 0, \quad \forall \boldsymbol{w} \in W_\mathcal{K},$$
$$-(\nabla\cdot(\rho\boldsymbol{u}),q)_\mathcal{K} + (f,q)_\mathcal{K} = 0, \quad \forall q \in Q_\mathcal{K},$$

where

$$W_\mathcal{K} := \left\{\boldsymbol{w} \in [L^2(\mathcal{K})]^2 : \nabla\cdot\boldsymbol{w} \in L^2(\mathcal{K}),\ \forall \mathcal{K} \in \mathcal{T}_h\right\} \quad \text{and} \quad Q_\mathcal{K} := \left\{q \in L^2(\mathcal{K}),\ \forall \mathcal{K} \in \mathcal{T}_h\right\}$$

are the local functional spaces, $\boldsymbol{n}_\mathcal{K}$ denotes the outward pointing normal to $\partial\mathcal{K}$, and $\hat{p}$ is the trace of pressure on Ω skeleton. We assume that κ is at least invertible element-wisely.

Then, the week formulation on each $\mathcal{K} \in \mathcal{T}_h$ reads as follows: find $(\boldsymbol{u},p) \in W_\mathcal{K} \times Q_\mathcal{K}$, such that

$$(\mu\kappa^{-1}\boldsymbol{u},\boldsymbol{w})_\mathcal{K} - (p,\nabla\cdot\boldsymbol{w})_\mathcal{K} - (\nabla\cdot(\rho\boldsymbol{u}),q)_\mathcal{K} + \langle\hat{p},\boldsymbol{w}\cdot\boldsymbol{n}_\mathcal{K}\rangle_{\partial\mathcal{K}} = -(f,q)_\mathcal{K}, \quad \forall(\boldsymbol{w},q) \in W_\mathcal{K} \times Q_\mathcal{K}.$$

Following the ideas of Arnold and Brezzi (1985), an approximation for the pressure trace can be obtained by solving the global problem corresponding to the dual hybrid mixed formulation: find $\boldsymbol{u} \in W := \prod_\mathcal{K} W_\mathcal{K}$, $p \in Q := \prod_\mathcal{K} Q_\mathcal{K}$, and $\lambda \in \mathcal{M} := \{\mu \in L^2(e),\ e \in \mathcal{E}_h\}$, such that

$$\sum\nolimits_{\mathcal{K}\in\mathcal{T}_h}\left[(\mu\kappa^{-1}\boldsymbol{u},\boldsymbol{w})_\mathcal{K} - (p,\nabla\cdot\boldsymbol{w})_\mathcal{K} + \langle\lambda,\boldsymbol{w}\cdot\boldsymbol{n}_\mathcal{K}\rangle_{\partial\mathcal{K}} + \langle p_D,\boldsymbol{w}\cdot\boldsymbol{n}_\mathcal{K}\rangle_{\partial\mathcal{K}\in\Gamma_D}\right] = 0, \quad \forall\boldsymbol{w} \in W, \tag{13}$$
$$\sum\nolimits_{\mathcal{K}\in\mathcal{T}_h}\left[-(\nabla\cdot(\rho\boldsymbol{u}),q)_\mathcal{K} + (f,q)_\mathcal{K}\right] = 0, \quad \forall q \in Q, \tag{14}$$
$$\sum\nolimits_{\mathcal{K}\in\mathcal{T}_h}\left[\langle\mu,\boldsymbol{u}\cdot\boldsymbol{n}_\mathcal{K}\rangle_{\partial\mathcal{K}} - \langle\mu,g_N\rangle_{\partial\mathcal{K}\in\Gamma_N}\right] = 0, \quad \forall\mu \in \mathcal{M}, \tag{15}$$

in which $\Gamma_D \subset \partial\Omega$ and $\Gamma_N \subset \partial\Omega$ ($\Gamma_D \bigcup \Gamma_N = \partial\Omega$ and $\Gamma_D \bigcap \Gamma_N = \varnothing$) are the sub-domains for pressure and flux boundary conditions, respectively.

The Lagrange multiplier λ is identified with the trace of the pressure on all edges of elements $\mathcal{K} \in \mathcal{T}_h$ satisfying the decomposition $\hat{p} = \lambda + p_D$, i.e., λ is solved for internal edges and p_D is prescribed on boundary edges (Cockburn et al., 2009; Nguyen et al., 2011). The third equation of (15), known as transmission condition (Cockburn et al., 2009), weakly imposes the continuity of the normal component of the Darcy velocity field (flux continuity). Note that flux boundary conditions are also weakly imposed through the transmission condition.

To obtain stable and (locally) adjoint consistent formulation, we add to the system (15) local stabilization terms associated with least square residual forms of the mass balance, Darcy's law, and the curl of Darcy's law (Correa and Loula, 2007), as well as the one for Lagrange multiplier (Arnold et al., 0102), i.e., $\forall \boldsymbol{w} \in W$, $\forall \mu \in \mathscr{M}$,

$$
\begin{aligned}
r_{\mathrm{MB}}(\boldsymbol{u},\boldsymbol{w}) &:= \delta_1(\|\kappa^{-1}\|_\infty(\nabla\cdot(\rho\boldsymbol{u})-f),\nabla\cdot(\rho\boldsymbol{w}))_{\mathscr{K}},\\
r_{\mathrm{D}}(\boldsymbol{u},\boldsymbol{w},p) &:= \delta_2(\mu\kappa^{-1}\boldsymbol{u}+\nabla p,\boldsymbol{w})_{\mathscr{K}},\\
r_{\nabla\times\mathrm{D}}(\boldsymbol{u},\boldsymbol{w}) &:= \delta_3(\|\kappa\|_\infty\nabla\times(\mu\kappa^{-1}\boldsymbol{u}),\nabla\times(\mu\kappa^{-1}\boldsymbol{w}))_{\mathscr{K}},\\
r_{\lambda}(\lambda,\mu,p) &:= \|\kappa\|_\infty\beta\langle\mu,\lambda-p\rangle_{\partial\mathscr{K}}.
\end{aligned}
$$

The Least-Squares weighting terms δ_i ($i=1,2$, or 3) values are based on Correa and Loula (2008), Loula et al. (2008), and Núñez et al. (2012). However, we modify δ_i to take into account local mesh-size h, following the ideas of Masud and Hughes (2002), when considering the mass balance residual term among stabilization mechanisms. Thus, we apply the mesh-dependent weighted Least-Squares (Bochev and Gunzburger, 1998) terms with $\delta_1=-1/2$ and $\delta_2=\delta_3=h^2/2$.

Then, the SDHM formulation reads as: find $\boldsymbol{u}\in W:=\prod_{\mathscr{K}}H^1(\mathscr{K})\times H^1(\mathscr{K})$, $q\in Q:=\prod_{\mathscr{K}}H^1(\mathscr{K})$, and $\lambda\in\mathscr{M}$, such that

$$
\begin{aligned}
\sum_{\mathscr{K}\in\mathscr{T}_h}\Big[&(\mu\kappa^{-1}\boldsymbol{u},\boldsymbol{w})_{\mathscr{K}}-(p,\nabla\cdot\boldsymbol{w})_{\mathscr{K}}+\langle\lambda,\boldsymbol{w}\cdot\boldsymbol{n}_{\mathscr{K}}\rangle_{\partial\mathscr{K}}+\langle p_D,\boldsymbol{w}\cdot\boldsymbol{n}_{\mathscr{K}}\rangle_{\partial\mathscr{K}\in\Gamma_D}\\
&+r_{\mathrm{MB}}(\boldsymbol{u},\boldsymbol{w})-r_{\mathrm{D}}(\boldsymbol{u},\boldsymbol{w},p)+r_{\nabla\times\mathrm{D}}(\boldsymbol{u},\boldsymbol{w})\Big]=0,\quad\forall\boldsymbol{w}\in W, \qquad (16)\\
\sum_{\mathscr{K}\in\mathscr{T}_h}\Big[&-(\nabla\cdot(\rho\boldsymbol{u}),q)_{\mathscr{K}}+(f,q)_{\mathscr{K}}+r_{\mathrm{D}}(\boldsymbol{u},\mathbb{K}\nabla q,p)-r_{\lambda}(\lambda,q,p)\Big]=0,\quad\forall q\in Q, \qquad (17)\\
\sum_{\mathscr{K}\in\mathscr{T}_h}\Big[&\langle\mu,\boldsymbol{u}\cdot\boldsymbol{n}_{\mathscr{K}}\rangle_{\partial\mathscr{K}}-\langle\mu,g_N\rangle_{\partial\mathscr{K}\in\Gamma_N}+r_{\lambda}(\lambda,\mu,p)\Big]=0,\quad\forall\mu\in\mathscr{M}, \qquad (18)
\end{aligned}
$$

where $\nabla\times$ is the curl operator and $\beta:=\frac{\beta_0}{h}\geq 0$ is the stabilization parameter with $\beta_0\in\mathbb{R}$.

The first and second equations in (18) generate the two local problems and the third the global problem. Then, we can approximate $\boldsymbol{u}$, p, and λ by approximations from the broken function spaces, i.e., $\boldsymbol{u}_h\in W_h^m:=\left\{\boldsymbol{w}_h\in\overline{W}:\boldsymbol{w}_h\big|_{\mathscr{K}}\in\mathbb{P}^m\times\mathbb{P}^m,\ \forall\mathscr{K}\in\mathscr{T}_h\right\}$, $p_h\in Q_h^l:=\left\{q_h\in\overline{Q}:q_h\big|_{\mathscr{K}}\in\mathbb{P}^l,\ \forall\mathscr{K}\in\mathscr{T}_h\right\}$, and $\lambda_h\in\mathscr{M}_h^s:=\left\{\mu_h\in\overline{\mathscr{M}}:\mu_h\big|_e\in\mathbb{P}^s,\ \forall e\in\mathscr{E}_h^0\right\}$, where W_h^m, Q_h^l, $\mathscr{M}_h^s$ are discontinuous Lagrangian finite element spaces. Here, $\mathbb{P}^k$ is the polynomial set with the degree less than or equal to k if $\mathscr{K}$ is a triangle or if e is an edge, or less than or equal to k in each Cartesian variable if $\mathscr{K}$ is a quadrilateral (here, $k=l$, m, or s). The SDHM method is consistent, provides optimal rates of convergence (Núñez et al., 2012), ensures flexibility of the approximation spaces choice, and locally conservative for equal order approximations of all fields (i.e., $l=m=s$). Moreover, the scheme is stable for any value of the edge stabilization parameter β , including $\beta=0$ (Núñez et al., 2012, 2017). Finally, the multiplier choice as the trace of pressure is crucial to ensure that the local problems are solvable for approximations $(\boldsymbol{u}_h,p_h)\in W_h^m\times Q_h^l$ as functions of the multiplier $\lambda_h\in\mathscr{M}_h^s$. Moreover, it results in a computationally efficient way to solve a global system with only the trace variable as unknown due to static condensation procedure.

Appendix B

The result of approximating the time derivative in (3) is the following sequentially implicit time-stepping scheme: for $k=1,\ldots,K-1$

$$\begin{array}{rcll} \frac{b^{k+1}-b^k}{\Delta t} + \nabla\cdot(\boldsymbol{v}b^{k+1} - D\nabla b^{k+1}) & = 0 & \text{in} & \Omega, \\ -(\boldsymbol{v}b^{k+1} - D\nabla b^{k+1})\cdot\boldsymbol{n}_{\text{inlet}} & = u\hat{b}_{in} & \text{on} & \Gamma_{\text{inlet}}, \\ -(\boldsymbol{v}b^{k+1} - D\nabla b^{k+1})\cdot\boldsymbol{n}_{\text{inlet}} & = 0 & \text{on} & \Gamma_{\text{top}}\cup\Gamma_{\text{bottom}}. \end{array} \tag{19}$$

To concentrate on the SUPG approximation scheme, we omit the index f indicating the amount of elements in the fluid species and the index $j = 1,\ldots,\text{E}$, numbering the elements. Then, the fully discrete approximation of (19) reads as: find $b^{k+1}\in X_h^p$ satisfying the bilinear form

$$B(b^{k+1},\eta) = F(b^{k+1},\eta), \quad \forall\eta\in X_h^p,$$

where

$$\begin{aligned} B(b^{k+1},\eta) &:= (b^{k+1},\eta) + \Delta t\,(\boldsymbol{v}\cdot\nabla b^{k+1},\eta) + \Delta t\,(D\nabla b^{k+1},\nabla\eta)_{\mathcal{K}} + S(b^{k+1},\eta), \\ F(b^{k+1},\eta) &:= (b^k,\eta) + (u\hat{b}_{\text{inlet}},\eta)_{\Gamma_{\text{inlet}}}, \end{aligned}$$

Here, we omit the sub-index of domain Ω in some of the L_2 inner-products, i.e., $(u,v)_\Omega \equiv (u,v)$, and assume the approximation space X_h^p to be a continuous Lagrangian finite element space of degree $p\geq 1$. The *stabilizing term* $S(b_h^{k+1},\eta)$ to the standard Petrov-Galerkin variational formulation is defined as

$$\begin{aligned} S(b^{k+1},\eta) := \sum_{\mathcal{K}} \tau_{\mathcal{K}}\Big((b^{k+1}-b^k) + \Delta t\,\boldsymbol{v}\cdot\nabla b^{k+1} - \Delta t\,\nabla\cdot(D\nabla b^{k+1}), \boldsymbol{v}\cdot\nabla\eta\Big)_{\mathcal{K}} \\ - \sum_{\partial\mathcal{K}\subset\Gamma_{in}} \tau_K(u\hat{b}_{\text{inlet}}, \boldsymbol{v}\cdot\nabla\eta)_{\partial\mathcal{K}\subset\Gamma_{\text{inlet}}}. \end{aligned}$$

with the stabilization parameter

$$\tau_{\mathcal{K}} := \begin{cases} \frac{h_{\mathcal{K}}}{2\|\boldsymbol{v}\|_{L^\infty(\mathcal{K})}} & ,\ \text{Pe}_{\mathcal{K}}\geq 1, \\ 0 & ,\ 0<\text{Pe}_{\mathcal{K}}<1. \end{cases}$$

It is dependent of the Peclet number $\text{Pe}_{\mathcal{K}} := d_{\mathcal{K}}\frac{m_{\mathcal{K}}\|\boldsymbol{v}\|_{L^\infty(\mathcal{K})}h_{\mathcal{K}}}{D_{\mathcal{K}}^2}$ with $d_{\mathcal{K}} := \alpha_{mol} + \alpha_t \inf_{\boldsymbol{x}\in\mathcal{K}}|\boldsymbol{v}(\boldsymbol{x})|$, $m_{\mathcal{K}} := \frac{2}{3}\min\left(\frac{1}{2}, c_{inv}\right)$, $D_{\mathcal{K}} := \left(2\big(\alpha_{mol}+\alpha_l\|\boldsymbol{v}\|_{L^\infty(\mathcal{K})}\big)^2 + 2\big(3\alpha_l - 2\alpha_t\big)^2\|\boldsymbol{v}\|^2_{L^\infty(\mathcal{K})}h^2_{\mathcal{K}}c_{inv}\right)^{1/2}$, where c_{inv} is the typical inverse constant of finite element spaces.

Appendix C

Below, we collect the plots showing the relative errors in minerals and aqueous species on the fixed reactive transport steps for both Cases I and II (see Figures 18 and 20). Moreover, using similar plots, we demonstrate that the balance equation $An = b$ is intrinsically satisfied in the approximations provided by the ODML algorithm (up to machine precision). In particular, Figures 19 and 21 confirm this property by illustrating relative errors of the balance conservation for the each of the elements used to generate the chemical systems in dolomitization and scavenging examples.

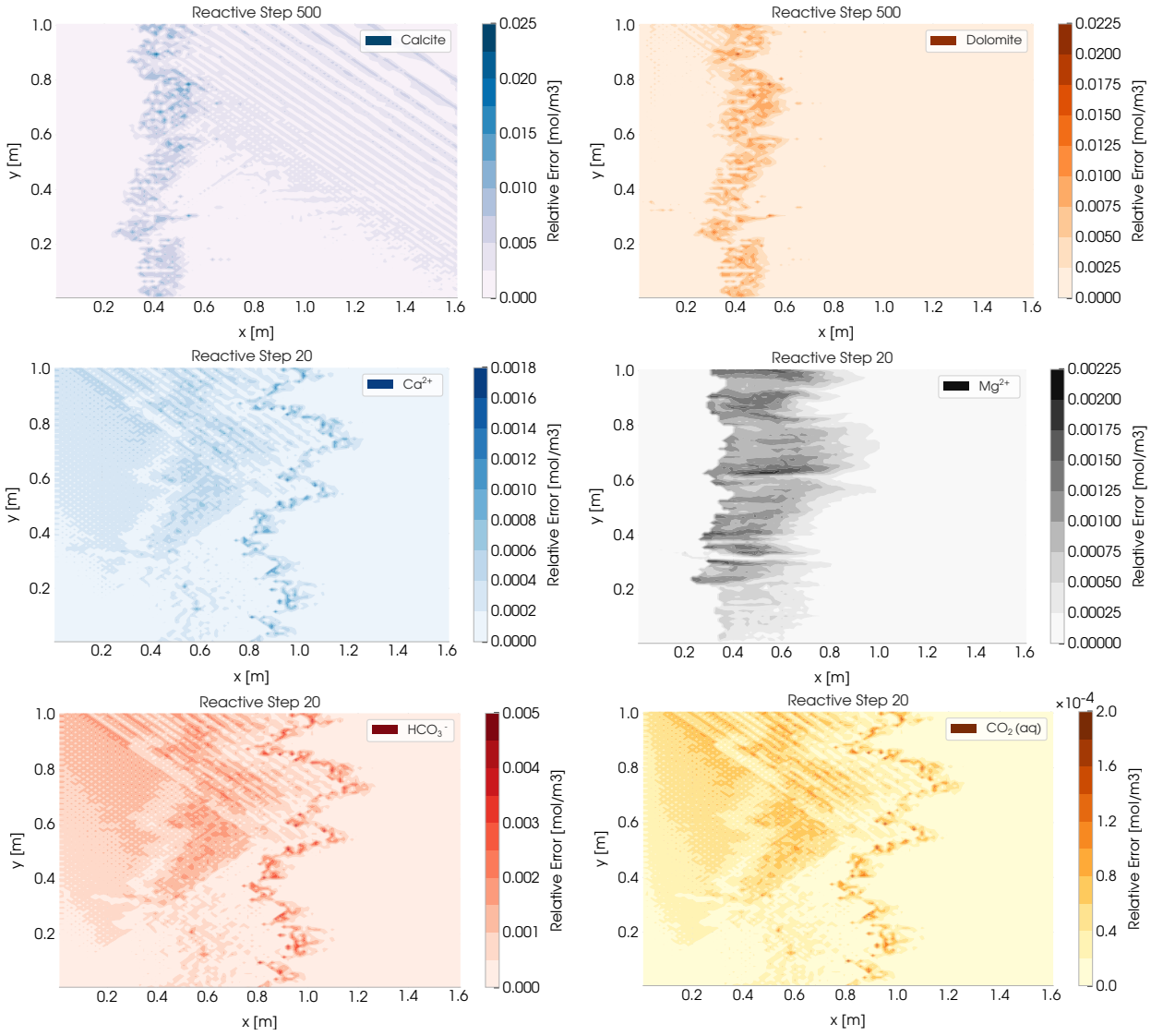


Figure 18: Relative error in minerals and several aqueous species on the fixed reactive transport steps in the dolomitization example. The ODML algorithm preformed with $\varepsilon = 0.001$.

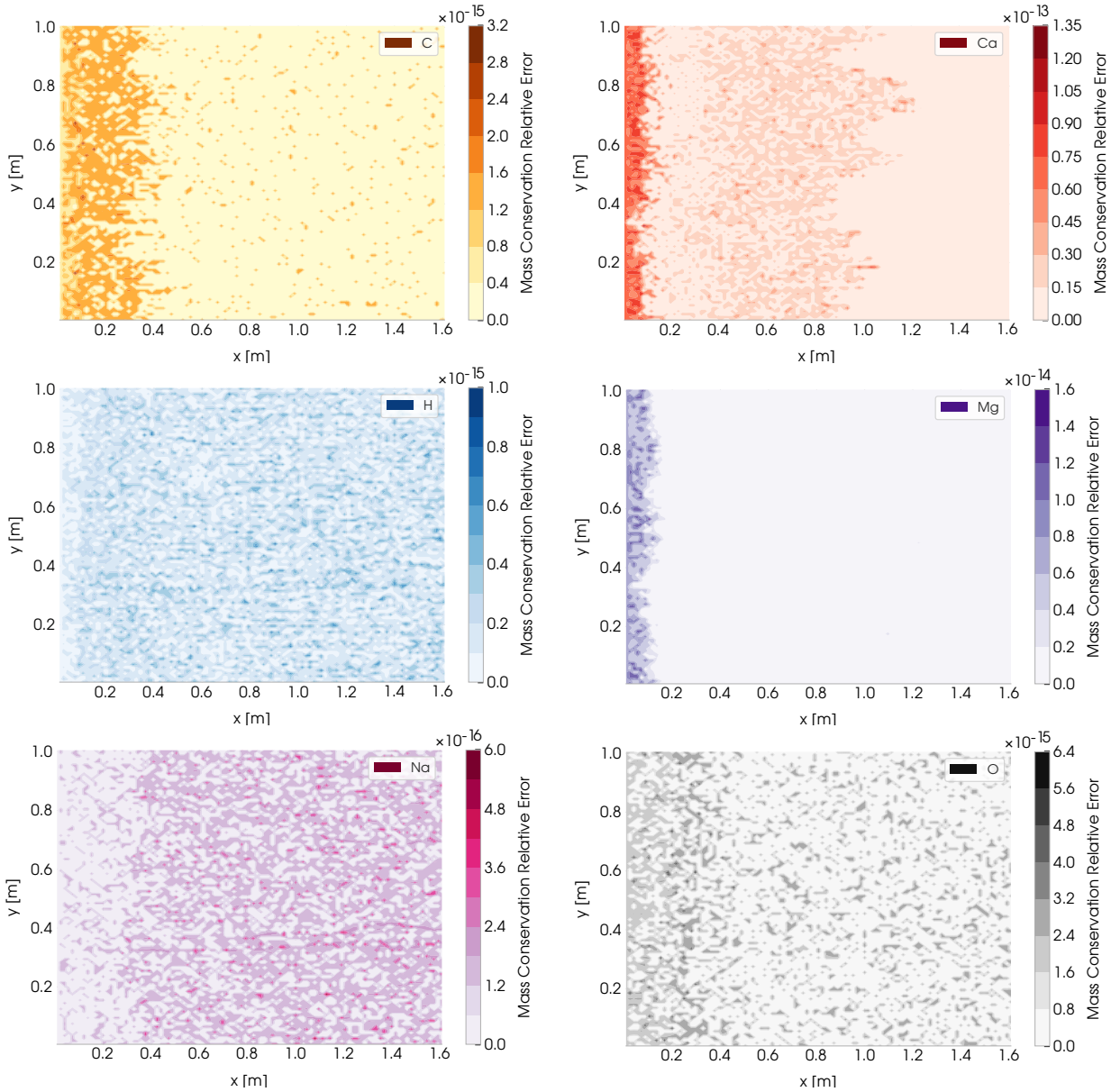


Figure 19: Relative error in the mass conservation equation for all the elements on the reactive step 1500 in the dolomitization example. The ODML algorithm preformed with $\epsilon = 0.001$.

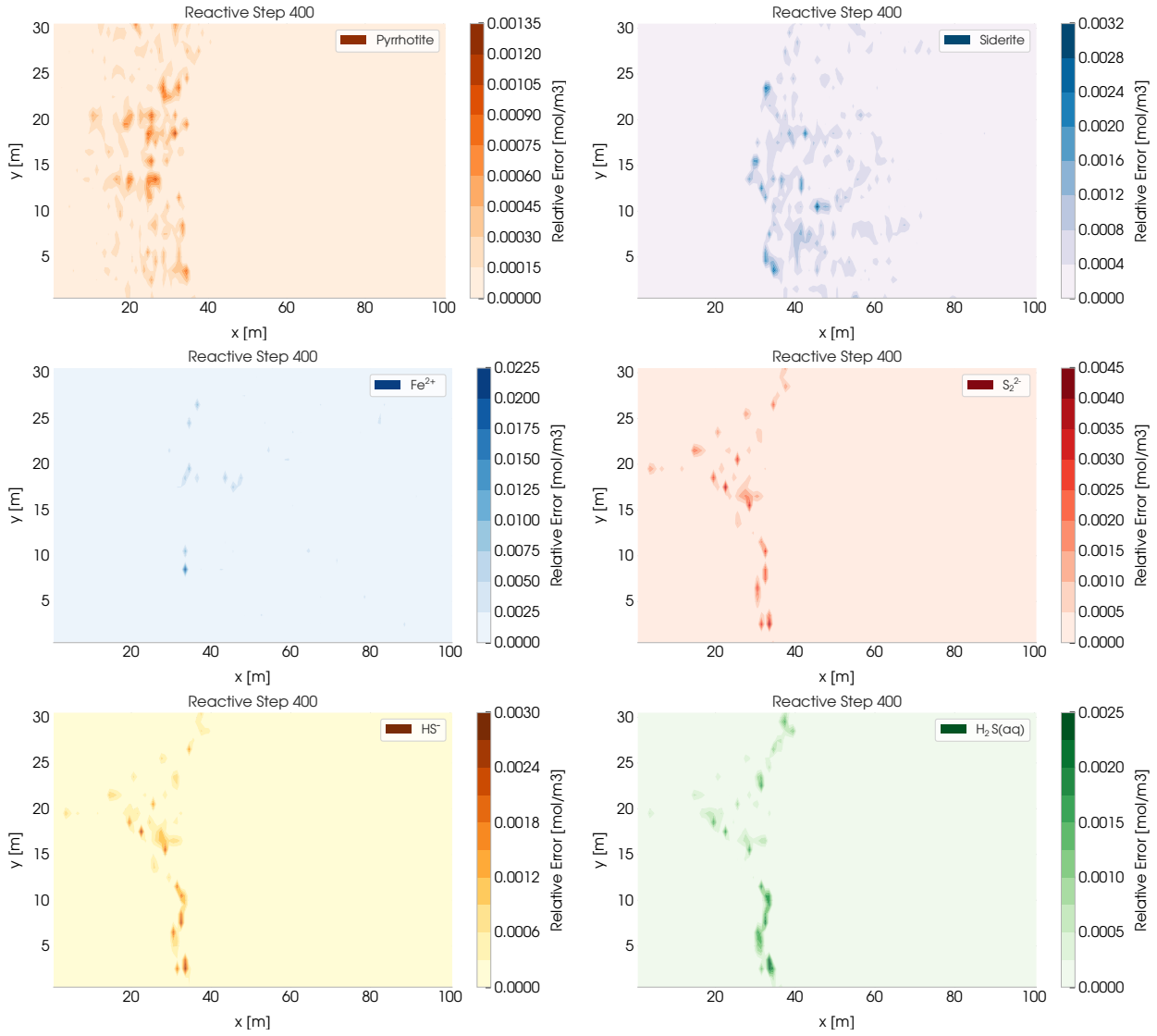


Figure 20: Relative error in minerals and several aqueous species on the fixed reactive transport steps in the H_2S-scavenging example. The ODML algorithm preformed with $\varepsilon = 0.001$

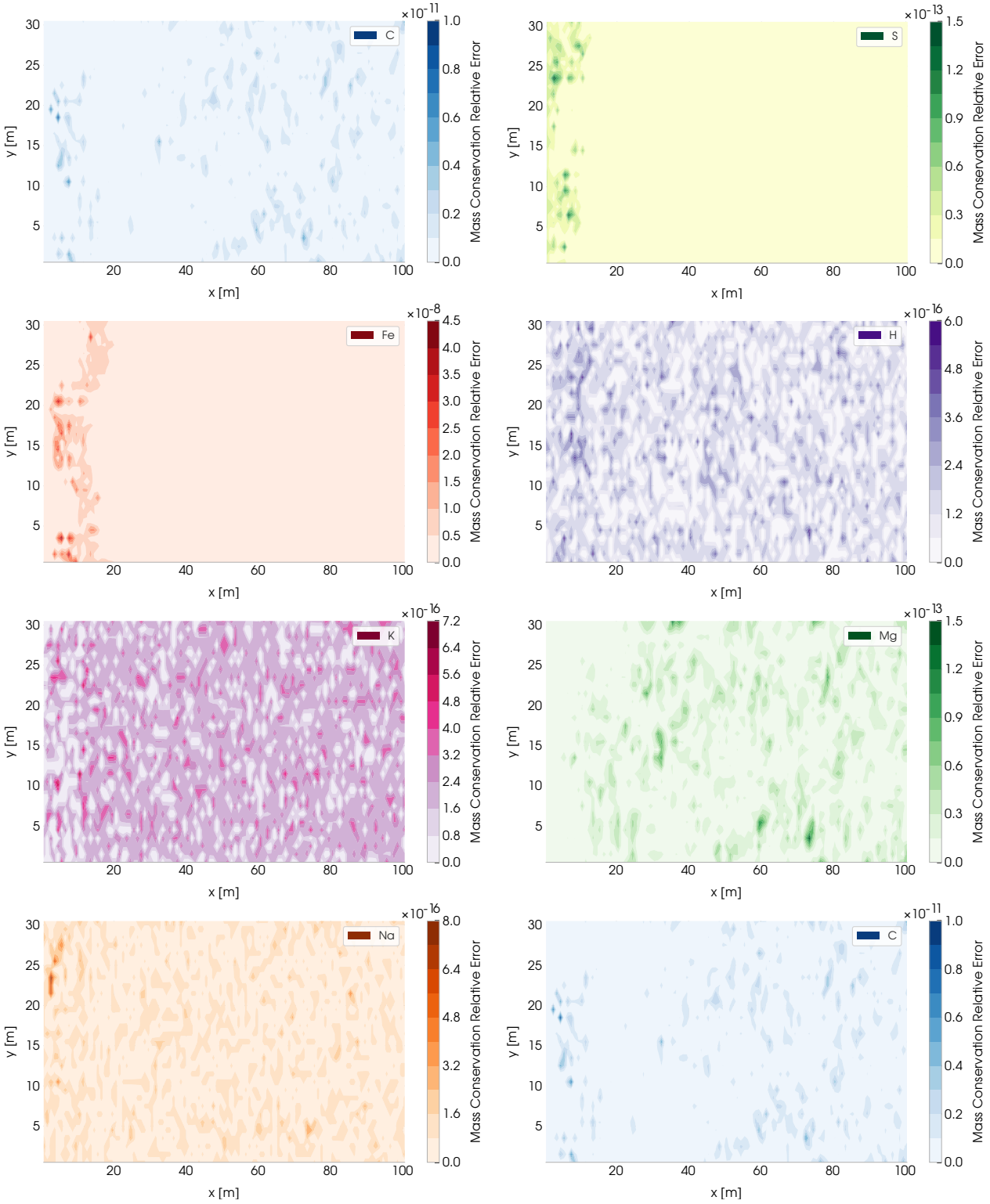


Figure 21: Relative error in the mass conservation equation for the selected elements on the reactive step 200 in the H_2S-scavenging example. The ODML algorithm preformed with $\varepsilon = 0.001$.